NEAR INFRARED LASER BEAM AND SILICON WAFER INTERACTIONS

by

Elif Türkan Akşit Kaya

B.S., Physics, Boğaziçi University, 2014

Submitted to the Institute for Graduate Studies in
Science and Engineering in partial fulfillment of
the requirements for the degree of
Master of Science

Graduate Program in Physics

Boğaziçi University

2019

ACKNOWLEDGEMENTS

I would first like to express my gratitude to my advisor Dr. Erkan Demirci at TÜBİTAK BİLGEM for his invaluable contributions to my knowledge for four years. Thanks to his advices and supports, I have gotten so much critical and significant experience on the electro-optic and laser systems laboratories at TÜBİTAK BİLGEM.

Additionally, I would like to thank Dr. Ramazan Şahin for his supports and guidance especially on theoretical analysis of my thesis. Besides, my colleagues showed patience and kindness for my studies in the laboratory during my research period, I am also indebted to all of them.

Furthermore, my advisor, Prof. Naci İnci, played a vital role in guiding me to choose optical studies during my undergraduate education at Boğaziçi University. I would like to thank him for his guidance.

Finally, I am truly grateful to my family, including my dear mother, my dear father, my dear siblings and my dear husband. Without their support, I would never be the person I am.

ABSTRACT

NEAR INFRARED LASER BEAM AND SILICON WAFER INTERACTIONS

At 1070 nm wavelength, Nanosecond (ns) pulse and Continuous Wavelength (CW) lasers' ablation of n-type(100) and p-type(111) Si wafer is presented in ambient, water and glycerin environments. Impacts of laser emission mode, pulse energy, pulse number, beam shape and type of environment are investigated by an Optical Microscope, a Scanning Electron Microscope and an Atomic Force Microscope. The integrating sphere measurements of optical reflection and transmission values are used in the calculation of the optical constant of the Si sample. Beam profiles acquired by a beam profiler and a CCD camera are presented before the experimental studies. Ablation zones are analyzed in terms of depth and diameter. Besides, temperature measurement of the samples under illumination by a CW laser at 1070 nm is given. In case of CW laser-induced damage regions, either partial molten or totally molten regions are observed along with the crack areas. After ns laser illumination, both the heat affected zones (HAZ) and the ablation zones are observed in ambient environment. Furthermore, in the HAZ area, some self-assembled ripple formations and re-solidified regions formed. However, in liquid environment, HAZ formation is observed to have reduced or completely disappeared. Bessel beam's declining effect on the HAZ area is also investigated after illumination of ns laser irradiation at 1070 nm. In all cases, regardless of medium and beam shape, the ablation diameter increases in line with the increments in pulse emission energies. Finally, through higher number of pulses, ablation craters with different depths are achieved with the same diameter of crater.

ÖZET

YAKIN KIZILÖTESİ LAZER HÜZMESİ VE SİLİSYUM ETKİLEŞİMLERİ

N-tipi(100) ve p-tipi(111) Si plakaların, 1070 nm dalgaboyunda nanosaniye (ns) ve sürekli modda (CW) lazer kaynakları ile ablasyon mekanizmaları hava, su ve gliserin ortamında incelenmiştir. Yapılan çalışmalar kapsamında, lazer emisyon modu, atım enerjisi, atım sayısı, hüzme şekli ve etkileşim ortamının lazer etkileşim üzerindeki etkileri ele alınmıştır. Oluşan ısıl etkileşim alanları ve ablasyon kraterleri Optik Mikroskop, Taramalı Elektron Mikroskobu ve Atomik Kuvvet Mikroskobu ile gözlemlenirken, deney esnasında hedef malzemenin ısınma ölçümleri uzun dalgaboylu kızılötesi kamera ile yapılmıştır. Toplama küresi ile ölçülen optik yansıtma ve geçirgenlik değerleri, Silikonun optik sabitlerini belirlemek için kullanılmıştır. Hüzme şekli CCD kamera ve hüzme görüntüleyici ile incelenip, ZEMAX analizleri ile bu tezde sunulmuştur. CW lazer etkileşim çalışmalarında, Si örneği üzerinde çatlak oluşumunun yanında, yarı-eriyik ve tam eriyik bölgeler oluştuğu gözlemlenmiştir. Ns atımlı lazer çalışmalarında ise, ısıl etkileşim alanları (HAZ) ve ablasyon alanlarının oluşmasının yanında, kendiliğinden oluşmuş dalgalı bölgeler ve eriyiklerin yeniden katılaşması ile oluşan omuzlar analiz edilmiştir. Ancak, sıvı ortamında ısıl etkileşim alanının azaldığı hatta tamamen yok olduğu gözlenmiştir. Bessel hüzmeleri ile yapılan çalışmalarda da ısıl etkileşim alanının azaldığı gözlenmiştir. Tüm çalışma sonuçlarına göre, lazer hüzme şeklinden ve test yapılan ortam türünden bağımsız olarak lazer enerjisindeki artışın ablasyon çapını arttırdığı gözlenmiştir. Bunun yanında, sabit bir enerji için lazer atım sayısının artması ile farklı derinliklerde fakat benzer çaplarda lazer ablasyon oluklarının oluşturulmasının mümkün olduğu görülmüştür.

TABLE OF CONTENTS

ACKNOWLEDGEMENTS iii
ABSTRACT iv
ÖZET v
LIST OF FIGURES viii
LIST OF TABLES xiv
LIST OF SYMBOLS xv
LIST OF ACRONYMS/ABBREVIATIONS xvii
1. INTRODUCTION 1
2. REVIEW 3
2.1. Lasers 3
2.2. Properties of Silicon as a Semiconductor 4
2.3. Laser-Material Interactions 5
2.3.1. Laser-Silicon Wafer Interaction 6
2.4. Laser Beam Profiles 11
2.4.1. Gaussian Beam Distribution 11
2.4.1.1. Focusing a Spherical Gaussian Beam 13
2.4.2. Bessel Beam Distribution 14
3. EXPERIMENTAL SECTION 17
3.1. Si Wafer Optical Properties Measurements 17
3.1.1. Optical Properties Measurement Technique 17
3.1.2. Reflection and Transmission Measurements 18
3.1.3. Optical characterization of Si wafer 20
3.2. Gaussian Beam Experiments in Different Media 22
3.2.1. Sample 22
3.2.2. Laser Sources 22
3.2.3. Analysis of Gaussian Beam 24
3.2.3.1. Theoretical Calculations 24
3.2.3.2. ZEMAX-EE Calculations 24
3.2.3.3. Beam Monitoring 26

3.2.4. Experiments in Different Media 27

3.2.4.1. Interaction in Ambient Medium 27

3.2.4.2. Interaction in Liquid Medium 34

3.2.4.3. Comparison of the Results 37

3.3. Bessel Beam Experiments 43

3.3.1. Sample 43

3.3.2. Laser Sources 43

3.3.3. Analysis of Bessel Beam 44

3.3.3.1. Theoretical Calculations 44

3.3.3.2. ZEMAX Calculations 45

3.3.3.3. Beam Monitoring 46

3.3.4. Experiments with Bessel Beams of Different Sizes 50

3.3.4.1. Interaction of Bessel Beam Produced by 1° Axicon Lens 51

3.3.4.2. Interaction of Bessel Beam Produced by 20° Axicon Lens 59

3.3.4.3. Comparison of the Results 65

4. CONCLUSION 69

REFERENCES 71

LIST OF FIGURES

Figure 2.1. Si wafer orientation based on doping type and wafer plane. 5

Figure 2.2. Absorption coefficient of a crystalline silicon within a range of 250 nm to 1450 nm [23]. 8

Figure 2.3. Laser induced ablation morphologies depending on the laser emission mode [25]. 9

Figure 2.4. An ablation zone after illumination with a ns pulse laser beam. . . 10

Figure 2.5. One directional Gaussian beam distribution in TEM_{00} mode (ZEMAX image). 11

Figure 2.6. ZEMAX illustration of focusing a Gaussian beam through a plano-convex lens. 13

Figure 2.7. Bessel beam formation through an axicon lens, simulated in ZEMAX. 15

Figure 2.8. One dimensional distribution of a Bessel beam. 16

Figure 3.1. Schematic of the RTC sphere used in optical properties measurements ([43]). 18

Figure 3.2. Pulse laser energy versus Q-switch delay and linear fit [measured by a pyroelectric energy meter (Ophir PE50-DIF-C)]. 23

Figure 3.3. A Gaussian beam distribution with 156 μm beam spot and normalized beam intensity in 3-D and 2-D views. 24

Figure 3.4. Nanosecond pulse laser beam horizontal profile in far field region. 26

Figure 3.5. 3-Dimensional nanosecond pulse laser beam shape in far field region. 27

Figure 3.6. Experimental setup in Gaussian beam experiments. 28

Figure 3.7. Temperature graph of p-type (111) Si wafer under illumination of 30 kW/cm^2 laser irradiance for 10 s. The temperature measurement was taken by LWIR thermal camera. 29

Figure 3.8. OM image of (100) n-type Si wafer surface after CW laser irradiation. 31

Figure 3.9. OM image of (111) p-type Si wafer surface after CW laser irradiation. 31

Figure 3.10. The angle between two cracks in n-type (100) (left) and p-type (111) (right) Si wafer after CW laser interaction. In n-type (100), the angle is 90° and in p-type (111) the angle is 60°. 32

Figure 3.11. Before the ablation process, the partially melted zone in n-type Si wafer (100) after CW laser illumination. 32

Figure 3.12. SEM image of a damage area after a single pulse interaction (18 mJ energy). Inner ring shows the ablation zone and outer ring shows the HAZ area. 34

Figure 3.13. SEM image of a ripple zone between ablation and HAZ area. (b) and (c) are zoomed areas from (a). The pulse energy is 50 mJ. . . 35

Figure 3.14. AFM topography of self-assembly ripples around ablation zone and HAZ for 50 mJ pulse energy. 36

Figure 3.15. Ablation zone diameter values of a p-type (111) Si sample based on the single pulse energy for a single pulse and multi-pulses studies. 37

Figure 3.16. OM false color images of laser applied damage areas based on the Q-switch adjustment level and the number of pulses. 38

Figure 3.17. Laser induced ablation zone of the Si(111) sample in water environment (SEM image). 39

Figure 3.18. Laser induced ablation zone of the Si(111) sample in glycerin environment (SEM image). 39

Figure 3.19. The effect of laser pulse energy on diameter square of ablation zones created on the Si(111) in water (a) and glycerin (b) medium. 40

Figure 3.20. SEM images of the ablation zones for different single pulse energies and different media. 41

Figure 3.21. Ablation depth of Si samples depending on the laser pulse energy and the medium type. 43

Figure 3.22. Bessel beam profiles in radial direction for different physical angles (left is 1° and right is 20°). 44

Figure 3.23. Transverse, longitudinal and spatial intensity graphs of Bessel beam after 1° axicon lens for 1070 nm wavelength. 45

Figure 3.24. Through-focus analysis in ZEMAX for a Bessel beam of 1° axicon lens (wavelength is 1070 nm). 46

Figure 3.25. Through-focus analysis in ZEMAX for a Bessel beam of 20° axicon lens (wavelength is 1070 nm). 46

Figure 3.26. ZEMAX image of the radial distribution of a Bessel beam produced by 20° axicon lens (wavelength is 1070 nm). 47

Figure 3.27. 3-D image of a Bessel beam produced by 1° axicon lens (wavelength is 1070 nm). 47

Figure 3.28. Transverse profile of the beam in Figure 3.27. 48

Figure 3.29. 20X magnification of the Bessel beam (1° axicon lens). 48

Figure 3.30. The transverse profile of a Bessel beam produced by 20° axicon at 633 nm wavelength (the graph contains the CCD image). 49

Figure 3.31. The CCD image of a Bessel beam produced by 1° axicon at 633 nm wavelength. 49

Figure 3.32. Experimental setup of Bessel beam-Si interaction studies. 50

Figure 3.33. Laser damaged zones of the Si wafer after the interaction with the Bessel beams of minimum (left) and maximum (right) energy values. 52

Figure 3.34. Ablation energy diameter vs pulse energy. 53

Figure 3.35. Ablation depth dependent on Bessel beam pulse energy. 53

Figure 3.36. SEM images of the ablation zones produced by 1, 40, 100, 1000 pulses at an energy level of 9.8 mJ. 54

Figure 3.37. Ablation diameter for different number of pulses. 55

Figure 3.38. Ablation depth for different number of pulses. 55

Figure 3.39. Ripple structures in the ablation zone on the surface of (111) p-type Si at a laser energy of 19.7 mJ 56

Figure 3.40. A sample damage area of the Bessel beam under water (pulse laser energy is 40 mJ). 57

Figure 3.41. Diameter of ablation zones vs laser pulse energy under water. . . . 58

Figure 3.42. Depth of the ablation crater vs pulse energy under water. 58

Figure 3.43. Damage areas produced by 1, 10, 100 and 1000 pulses. Bessel beam energy is 9.8 mJ. 59

Figure 3.44. Diameter of the ablation zone vs. number of pulses in water ambient. 60

Figure 3.45. Depth of the ablation zone vs. the number of pulses in water ambient. 60

Figure 3.46. AFM image of the minimum ablation area on the Si sample surface after illumination with Bessel beam (20° axicon). 61

Figure 3.47. 2-D and 3-D AFM images of the maximum ablation area on the Si sample. 62

Figure 3.48. Ablation diameters vs. Bessel beam pulse energies. 62

Figure 3.49. Depths of ablation zones vs. Bessel beam pulse energies. 63

Figure 3.50. SEM images of ablation zones for different number of pulses at 14 mJ. 63

Figure 3.51. Diameters of ablation zones vs. the number of Bessel beam pulses. 64

Figure 3.52. Depths of ablations vs. the number of Bessel beam pulses. 64

Figure 3.53. OM images of Bessel beam induced ablation zones in ambient and water media 66

LIST OF TABLES

Table 3.1. ZEMAX Optical Design Program Lens Data Editor Parameters . . 25

Table 3.2. Water and Glycerin material properties used as inputs in the ZEMAX 25

Table 3.3. Physical properties of Water and Glycerin 40

LIST OF SYMBOLS

A	Absorbance
C	Celsius
f	Focal length of the lens
I_0	Peak intensity of the laser source
k	Extinction coefficient
M^2	Beam Propagation Ratio
n	Refractive index
P	Power of the laser source
R	Reflection
R_d	Reflection's diffuse part
R_s	Reflection's specular part
R_t	Reflection - Total
s	The length between the lens and the laser source before the lens
s'	The length between the lens and the laser source after the lens
S_{dark}	Noise of the integrating sphere detector
$S_{Std}(\lambda)$	The detector value for the reflection standard sample measurement
$S_S(\lambda)$	The detector value for the specimen measurement
T	Transmission
w	Beam radius
w_0	Beam waist of Gaussian beam
w_{ff}	Beam radius at far field
z	The symbol of laser propagation direction
z_R	Rayleigh range of focused beam
α	Absorption coefficient
ϵ	Dielectric constant

λ	Laser wavelength
θ	Beam divergence

LIST OF ACRONYMS/ABBREVIATIONS

2-D	Two-Dimensional
3-D	Three-Dimensional
CW	Continuous Wavelength
AFM	Atomic Force Microscope
CCD	Charge Coupled Device
cm	Centimeter
D	Diameter of the beam
EDX	Energy Dispersive X-ray
EFM	Electron Force Microscope
eV	Electron Volt
FOV	Field of View
HAZ	Heat Affected Zone
HeNE	Helium Neon laser
Hz	Hertz
LIDT	Laser Induced Damage Threshold
LWIR	Long Wavelength Infrared
MFM	Magnetic Force Microscope
mJ	milliJoule
mm	Millimeter
mW	milliWatt
MW	MegaWatt
n-type	Phosphorus doped Silicon wafer
Nd-YAG	Neodymium-doped Yttrium Aluminum Garnet
nm	NanoMeter
ns	NanoSecond
O	Oxygen
OM	Optical Microscope
ps	PicoSecond

PSI	Phase Shifting Interferometry
p-type	Boron doped Si wafer
RTC	Reflectance and Transmittance sphere
SEM	Scanning Electron Microscope
Si	Si
μm	Micrometer
VSI	Vertical Scanning Interferometry
W	Watt
xxX	Magnification ”xx” times

1. INTRODUCTION

Laser induced surface machining has a great importance in different industrial areas ranging from medical technologies [1] to defense and security systems [2] since it gives opportunities of non-contact surface modifications on samples in concern. On the other hand, laser-surface texturing brings an opportunity of the nano- or micro-scale engineering [3]. Laser ablation quality mainly depends on pulse duration. In ultrafast regimes (picosecond, femtosecond, etc.), laser energy yields an ablation zone by breaking only the chemical bonds of the samples [4,5]. However, if the pulse duration gets closer to heat diffusion time, the energy of laser source leads to temperature rise and heat diffusion over the surface [6]. Furthermore, when the laser emission duration is longer (microsecond, continuous), the crystalline planes slip based on sample type before ablation takes place [7]. Nevertheless, there are so many parameters in the laser ablation mechanisms of the samples in terms of laser characteristics and material properties.

Surface engineering in the crystalline Si specimen is a significant phenomenon, because the way of patterning its surface plays an important role on its performance [8, 9]. Previously, so many surface modification studies of Si specimens were carried under ultrafast laser illuminations [10–12] in order to get rid of the thermal effects of a laser source. Moreover, in case of ns laser regime, most of the laser induced Si ablation studies were performed by UV and visible ranges [13, 14]. However, a nanosecond laser source is cheaper than an ultrafast laser system, and it yields smaller ablation zones than a CW laser does. Besides, the needs of the industry for Si surface micromachining can be satisfied with nanosecond lasers [15]. On the other hand, infrared laser beam (at 1070 nm) does not require any harmonic generation, which increases the cost efficiency in the fabrication process. Also, the photon energy of 1070 nm laser beam is a little bigger than the band gap energy of Si, therefore, surface texturing can be performed systematically. On the other hand, the thermal impacts of a ns laser source on a mono crystalline Si sample can be extinguished due to a denser interaction media [16].

This study mainly aims at observing the differences in the optical and structural characteristics of various mono-crystalline Si wafers after inducing a laser light with different emission modes. Additionally, this study encompasses the heat affected zone reducing techniques under illumination of a nanosecond pulse laser.

This thesis consists of four chapters: The second chapter presents brief information about lasers and silicon wafer as well as laser-matter interaction mechanisms. The third chapter addresses the methodologies used in the measurements and experimental studies. Following the presentation of the measured optical properties of the Si wafer, the experimental studies are explained, and the results are given. The experimental studies are divided into two main parts with respect to the beam shapes including the Gaussian and Bessel beam profiles, which is followed by the surface analysis. Finally, the last chapter offers the conclusion and suggestions for future works.

2. REVIEW

2.1. Lasers

Since their first introduction in the 1960s, lasers have played significant roles in technological developments. Especially, in so many sub-fields of science, medicine, industry, information technology and military, lasers have been offering great improvements at a remarkable speed day by day. The laser technology, itself, has also developed in terms of such specifications as average output power, wavelength band, emission duration, etc. According to emission durations, lasers have two main modes: continuous and pulsed. In continuous wave (CW) mode, the output power of laser beam does not change as the laser operates. On the other hand, the pulsed laser works according to this principle: The pulse laser emission occurs in a specific time duration at a specific repetition rate. If the pulse duration of a laser beam is equal to or less than a picosecond (ps), the laser system is called ultrafast laser. There is also a fast laser regime with a pulse duration of approximately one nanosecond (ns) or above. In the fast pulse laser system with nanosecond pulse duration, there is a Q-switched operation which produces intense short laser pulses. Basically, a Q-switched system works as described below:

- While pumping the gain medium, laser light emission is prevented by high resonator losses. This process can be achieved thanks to active or passive Q-switching techniques.
- By reducing the resonator loss suddenly, gain gets higher than the losses, and the optical power occurs sharply and intensely until the gain is saturated.

Moreover, according to the gain medium type of the laser source, the lasers can be categorized as gas lasers, solid state lasers, fiber lasers, etc. The feature of the gain medium is very important in terms of the excited laser beam wavelength. The most commercial laser is probably the HeNe gas laser which can work at different wavelength regions continuously and coherently, but it is generally used at a wavelength of 633

nm [17]. In material processing with laser systems, namely laser cutting [18], laser drilling [19] and laser micro-machining [20], fiber lasers are mostly used nowadays.

2.2. Properties of Silicon as a Semiconductor

Although the second most abundant element of the Earth crust is Silicon (Si), it cannot be found as a pure element in the crust because of its affinity to oxygen. Silicon has a wide range of application areas from cosmetics to electronics. Silicon wafers have acquired an important place in the semiconductor (SC) industry [21]. Because of its band gap energy (1.12 eV), Si can withstand temperatures up to 200°C, which provides many advantages to Si as a semiconductor over other materials such as Germanium.

Si wafers may differ from each other according to their characteristics in terms of crystalline structure, purity and doping type. The crystal structure of a Si wafer is a diamond cubic lattice, and the wafer crystal plane is defined by Miller indices with (hkl) notation. Moreover, in order to achieve free charge carriers on semiconductors, doping elements are used. In other words, since the doping element decreases the band gap energy of the semiconductor substrate, the doped wafer can be greatly effective to conduct the electricity even at room temperature. There are two main kinds of dopant, namely n-type and p-type. In case of n-type doped Si wafer, such donor elements as Phosphorus, Arsenic and Antimony are used in order to increase the conductivity of Si wafers through free electrons. Furthermore, p-type Si wafer, which means doped with such acceptor elements as Boron, Aluminum and Gallium, has more holes than the intrinsic Si substrate. Si wafers are formed in accordance with their types and orientations, as can be seen in Figure 2.1.

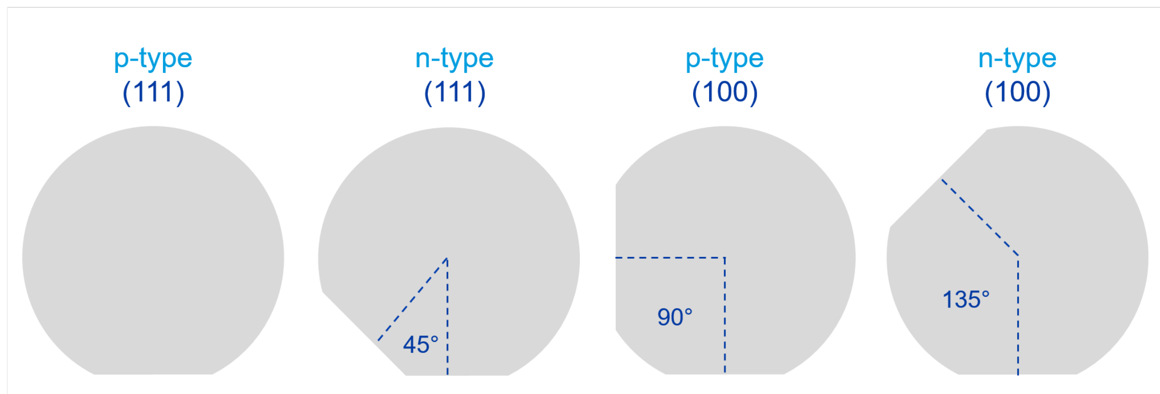

Figure 2.1. Si wafer orientation based on doping type and wafer plane.

2.3. Laser-Material Interactions

Laser-material interaction depends on two main parameters: laser properties and material properties. In terms of laser characteristics,

- laser wavelength,
- laser emission mode,
- application time,
- beam diameter,
- beam shape,
- intensity,
- polarization,
- angle of incidence

all play a significant role in material processing. On the other hand, in terms of material characteristics,

- chemical composition of a sample,
- optical and physical properties of a sample,

- material dimensions,
- surface topography,
- surface purity,

can be listed as the main elements playing a role in the interaction mechanism. Furthermore, the surface processing capacity of a laser also depends on the environmental conditions [22]. Media type, atmospheric impurities, turbulence, temperature, humidity and the gas' composition may be listed as the major agents in the interaction quality.

2.3.1. Laser-Silicon Wafer Interaction

When a light beam falls upon a matter, there are three main probabilities: reflection, transmission and absorption. For a pure semiconductor (SC), if the material band gap energy is bigger than the photon energy, the absorption does not occur. In case of a crystalline silicon, when the photon energy satisfies the relation given in equation 2.1, band-to-band absorption occurs.

$$\frac{hc}{\lambda} > E_g \tag{2.1}$$

Where the hc is the multiplication of the Planck's constant and the speed of light in vacuum, and its value is 1240 eV.nm, and the λ is the wavelength of the laser beam. There are two types absorption mechanisms in the interband transition for a crystalline Si:

- Direct transition: the energy between the valence band and the conduction band with the same wave vector. Silicon direct transition band gap is 3.4 eV
- Indirect transition: the energy between the valence band and the conduction band with different wave vectors. This is the Silicon's fundamental band gap, and its value is 1.12 eV.

In any medium, the laser beam propagation can be defined by the Beer-Lambert law (Equation 2.2). According to the law, a laser beam loses its initial intensity (I_0) exponentially based on the material absorption coefficient (α) and the distance (z) covered by the light after passing through the media. The absorption coefficient of the Si wafer depending on the laser wavelength in a range of 250 nm to 1450 nm is given in Figure 2.2.

$$I(z) = I_0 e^{-\alpha z} \tag{2.2}$$

If the laser-induced excitation time is lower in comparison to thermalization time, being a material characteristic, absorbed energy directly transforms into the heat (photothermal interaction). Conversely, when the laser-induced excitation time is higher than the thermalization rate, absorbed energy is enough to fracture the chemical bonds (photochemical interaction) [24] without any thermal effect. Hence, according to the laser emission mode, the ablation of a sample shows various morphologies as can be seen in Figure 2.3. In Continuous wavelength (CW) laser emission case, the interaction is photothermal and the laser-induced damage area covers heat affected zones containing re-solidified regions and re-deposited formations. However, in case of a nanosecond (ns) pulse laser source, even if there is heat diffusion in the material, heat affected zone is smaller than the CW laser effect and is limited due to the short duration of the pulse.

Since the crystalline Si has a widespread application area, it always draws attention in studies on laser induced surface modification. For years, different types of lasers have been used in order to texture the surface of Si wafer [26–28] with different pulse lasers. Furthermore, surface texturing of crystalline Si is significant in terms of developing its optical properties [24]. Specifically, yielding a ”black silicon” enhances the Si absorption dramatically by lowering its reflection [29]. Although there are different techniques to produce a ”black silicon” [29–31], laser-induced texturing with a ns laser beam in gas medium brings low cost and high efficiency [32]. Moreover, yielding cracks or partial melting regions in Si wafers by using the low laser irradiance of a CW

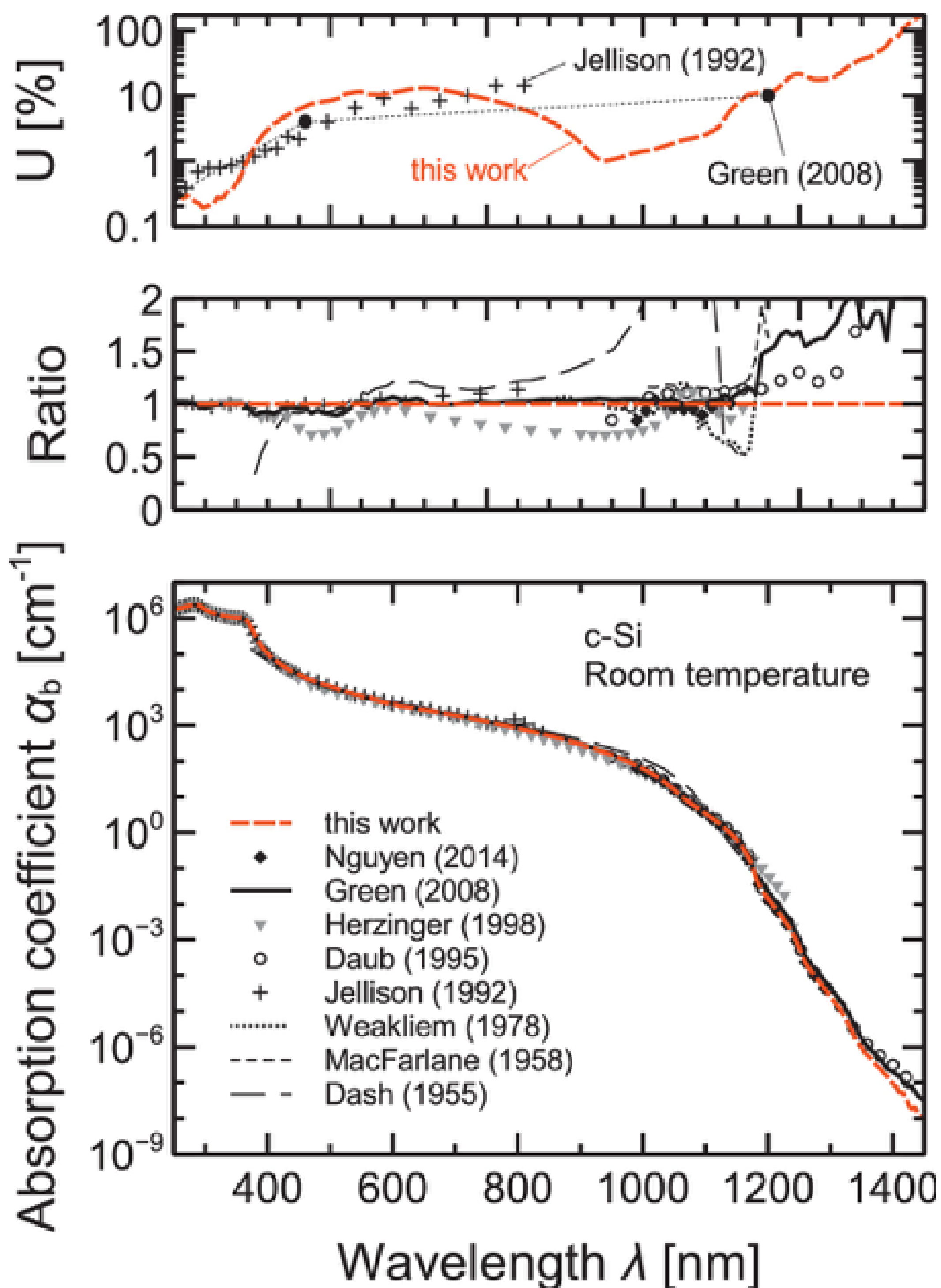

Figure 2.2. Absorption coefficient of a crystalline silicon within a range of 250 nm to 1450 nm [23].

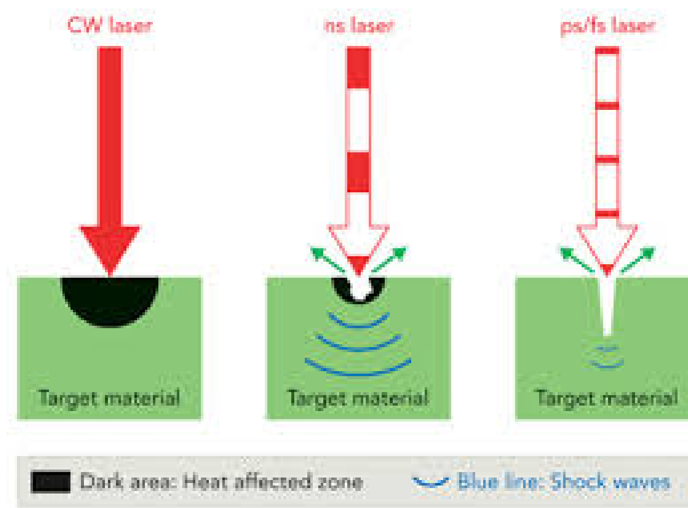

Figure 2.3. Laser induced ablation morphologies depending on the laser emission mode [25].

laser source is a fundamental progress for applications in the security field, because crystalline Si wafers are used as detectors or sensor chips in military devices [33].

Laser-induced Si wafer interaction may be categorized according to laser emission mode, beam shape and application environment. After illumination of a CW laser beam, depending on the intensity of the laser source and the properties of the Si wafer, the material demonstrates different damaged regions. Just before the melting in the ablation zone under laser exposure, Si wafer planes may slip based on the wafer orientation and doping level [34]. The same behaviour can also be seen in the crystalline Si wafers after microsecond laser irradiation [7,35]. Yet, in case of the ns laser ablation of Si wafer, the ablation mechanism changes, thereby producing a lower HAZ area and smaller ablation zones (Figure 2.4), in comparison to a CW laser system.

Pulse laser induced damage areas can be examined based on the beam diameter and the number of pulses. For a Gaussian beam, the relationship of the ablation diameter (D) square with the laser beam radius (w_0) and the laser fluence (F) is shown in the Equation 2.3. While E is the energy of the laser, the maximum fluence

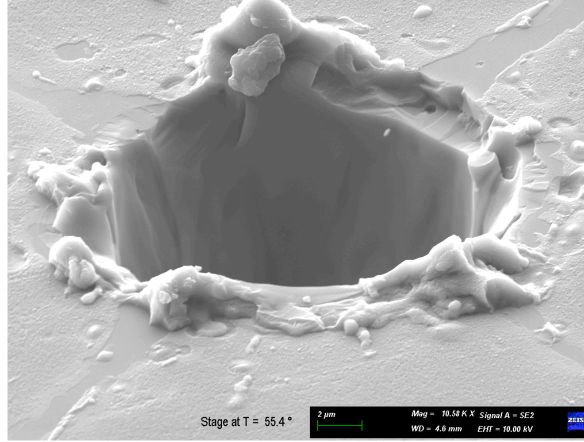

Figure 2.4. An ablation zone after illumination with a ns pulse laser beam.

of the Gaussian beam can be expressed by $2E_0/\pi w_0$.

$$D^2 = 2w_0^2 \left(\frac{F_0}{F_{th}} \right) \tag{2.3}$$

By plotting the natural logarithmic graph of the laser fluence and ablation diameter square, the beam diameter and the damage threshold can be ascertained from the slope of the graph and its intersection point respectively. However, this equation is mostly used in ultrafast pulse regimes [36, 37], because the thermal effects are still accurate for a ns laser [38]. Yet, in a liquid medium, since the thermal effects of laser radiation on the surface decrease or even disappear completely [16], the equation can be rearranged in a way to make it useful for ns pulse laser-Si material interaction analysis [38]. Moreover, the number of laser pulse has a significant impact on the laser-material interaction since it produces more controlled ablation structure with smaller pulse laser energy [39]. Additionally, multi-pulses interaction may create ablation zones even with sub-threshold laser emission energies. Besides, laser beam shape affects the laser fluence, because the shape is directly related to the distribution of the beam intensity in transverse direction. To compare the Bessel beam with the Gaussian beam, the former has deeper focal depth than the latter [40], providing the opportunity of controlled surface machining of the material without the need for sampling and concerns of proper placing. Also, a Bessel beam with enough energy may ablate the

sample by using only the center lobe. In other words, the rings of the Bessel beam do not contribute to the ablation structure, hence, the micro- [41] and nano-dimensional fabrication can be easier.

2.4. Laser Beam Profiles

2.4.1. Gaussian Beam Distribution

The Gaussian beam profile means that the laser beam has radially symmetric distribution (Figure 2.5).

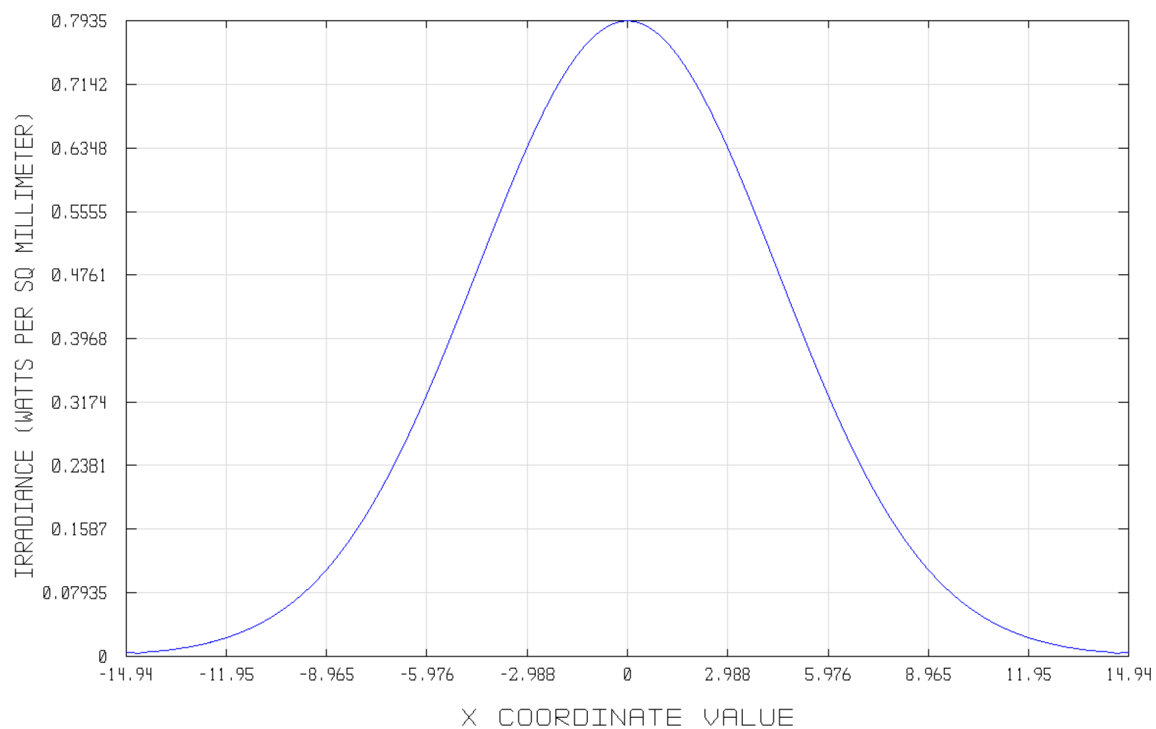

Figure 2.5. One directional Gaussian beam distribution in TEM_{00} mode (ZEMAX image).

The TEM_{00} mode theoretically gives the main Gaussian distribution. The irradiance distribution of the TEM_{00} mode is,

$$I(r,z) = I_0 * e^{\frac{-2r^2}{w^2}} = \frac{2P}{\pi w^2} * e^{\frac{-2r^2}{w^2}}. \tag{2.4}$$

where the beam radius w ($1/e^2$ (13.5%) of the intensity on axis) is

$$w(z) = w_0 \sqrt{1 + (\frac{z}{z_R})^2}. \tag{2.5}$$

Where the w_0 is the beam radius at the waist ($z = 0$) and the z_R is the Rayleigh range, so

$$z_R \equiv (\frac{\pi w_0^2}{\lambda}). \tag{2.6}$$

Based on the Rayleigh range, the near field and far fields are determined by the following relations:

$$\begin{aligned} &\text{if} \quad z_R > z \quad \text{near field,} \\ &\text{if} \quad z_R < z \quad \text{far field.} \end{aligned}$$

In the far field, the beam radius is

$$w_{FF} \rightarrow w_0(z/z_R) = \frac{\lambda z}{\pi w_0}. \tag{2.7}$$

In addition, in the far field, the half-angle divergence is

$$\theta_{FF} = w_{FF}/z = \frac{\lambda}{\pi w_0}. \tag{2.8}$$

Moreover, the beam quality factor, namely M^2 factor, also has an effect on the divergence angle. In case of a diffraction limited beam, the M^2 of the beam equals to 1, and

it is a Gaussian beam in TEM_{00} mode. This is the lowest value that a beam quality can have. Beam divergence is also affected by the M^2 factor, which restricts the degree of beam focusing. Therefore, the beam divergence angle can be rewritten as:

$$\theta_{FF} = M^2 \frac{\lambda}{\pi w_0}. \tag{2.9}$$

2.4.1.1. Focusing a Spherical Gaussian Beam. The Gaussian beam can be focused through an optical lens system as shown in Figure 2.6. Laser beam radius is theoretically calculated by using the equations below [42].

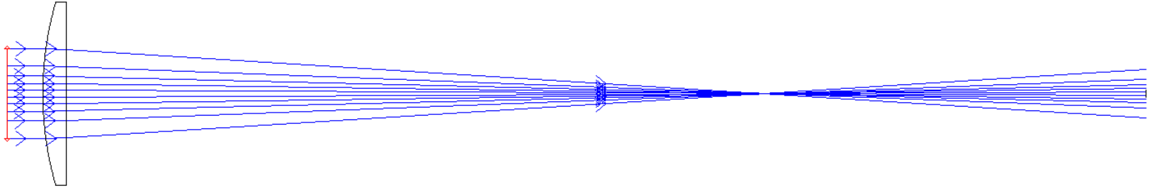

Figure 2.6. ZEMAX illustration of focusing a Gaussian beam through a plano-convex lens.

Using the Gaussian beam formula, the geometrical lens formula for a Gaussian beam can be written as:

$$\frac{1}{s + \frac{z_R^2}{s-f}} + \frac{1}{s'} = \frac{1}{f} \tag{2.10}$$

where s is the distance between the beam waist radius before the lens and the location of the lens; s' is the distance between the beam waist radius after the lens and the location of the lens, and f is the focal length of the lens. After normalization of the

formula, it becomes:

$$\frac{1}{\frac{s}{f}+\frac{\frac{z_R}{f}^2}{\frac{s}{f}-1}}+\frac{1}{\frac{s'}{f}}=1 \tag{2.11}$$

Furthermore, the magnification factor is:

$$m=\frac{w_0'}{w_0}=\frac{1}{\sqrt{[1-\frac{s}{f}]^2+(\frac{z_R}{f})^2}} \tag{2.12}$$

The magnification factor is used to calculate the focused laser beam spot size after the collimated laser beam passes through the plano-convex lens.

Furthermore, for a laser beam with $M^2 = 1$, the focused beam diameter (w_0') can also be expressed by the relation among D (diameter of the incoming beam), f (focal distance of the lens) and λ (wavelength of the laser):

$$w_0'=\frac{4\lambda}{\pi}\frac{f}{D} \tag{2.13}$$

Additionally, the depth of focus of the beam is given in the equation 2.14.

$$DOF=\frac{8\lambda}{\pi}\left(\frac{f}{D}\right)^2 \tag{2.14}$$

2.4.2. Bessel Beam Distribution

A Bessel beam is the laser beam that propagates through the medium without diffraction and losing its intensity. Ideally, a Bessel beam consists of infinite number of rings with same energy levels. An ideal Bessel beam electric field equation is [40]:

$$E_m(r,\phi,z)=A*e^{ik_z z}J_m(k_r r)*e^{im\phi} \tag{2.15}$$

where J_m, k_z and k_r are the longitudinal and radial wave vectors of mth degree Bessel beam. In the experiments we used first degree Bessel beams. k can be given by:

$$k = \frac{2\pi n}{\lambda} = \sqrt{k_z^2 + k_r^2} \tag{2.16}$$

A Gaussian beam can be converted into a Bessel beam through different techniques such as using an axicon lens or a hole with the diameter of Gaussian beam. This kind of Bessel beam is called Gaussian Bessel. In Figure 2.7, a ZEMAX image shows the reshaping of a Gaussian beam to a Bessel beam by an axicon lens (base angle is 1°). The Gaussian Bessel beams consist of a central peak lobe and co-energetic rings with

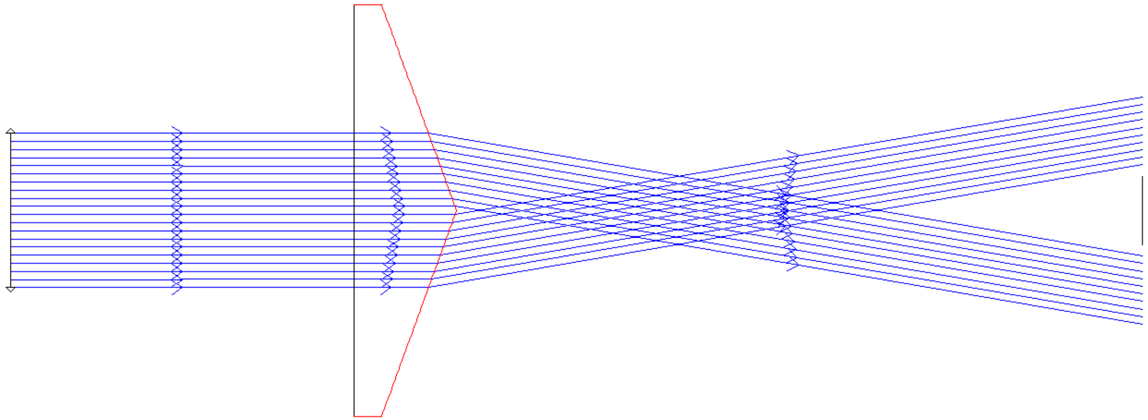

Figure 2.7. Bessel beam formation through an axicon lens, simulated in ZEMAX.

co-central distribution. In theory, the number of rings in a Bessel beam and the length of Bessel zone are both infinite. However, in reality, this is not possible, because it requires infinite energy distribution. Figure 2.8 shows a real Bessel beam distribution executed by ZEMAX optical design program.

Therefore, the Bessel distribution of a beam is observed in a finite range (z_0):

$$z_0 = w_0 \frac{k}{k_r} = \frac{k}{2.405} w_0 r_0 \tag{2.17}$$

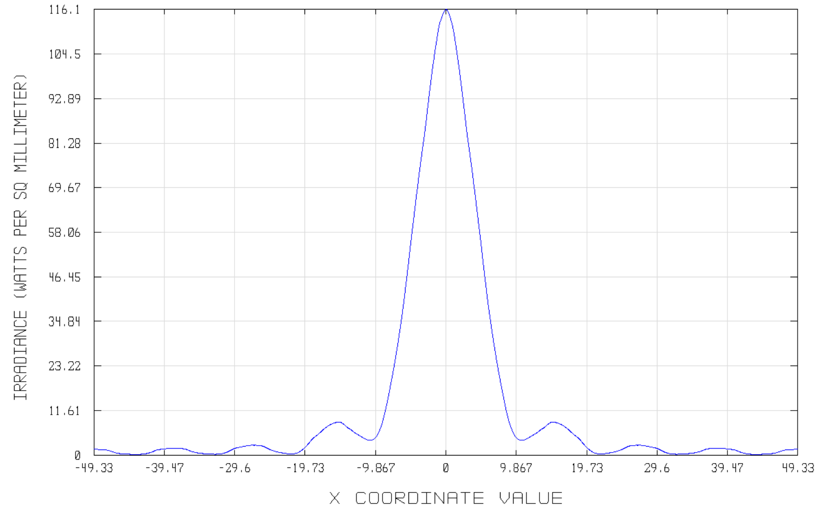

Figure 2.8. One dimensional distribution of a Bessel beam.

Where the w_0 is the Gaussian beam's radius, and the r_0 is the center lobe radius and can be calculated by:

$$r_0 = \frac{2.405}{k_r} \tag{2.18}$$

As can be seen in Figure 2.7, in far field ($z > z_R$), the Bessel beam propagates as a unique ring.

3. EXPERIMENTAL SECTION

3.1. Si Wafer Optical Properties Measurements

3.1.1. Optical Properties Measurement Technique

The Sample's optical properties, being reflection (R) and transmission (T), are measured by using an integrating sphere. Particularly, Labsphere's instrument called RTC-0533-SL reflectance and transmittance assembly was used in this research. Inner coating of the sphere is spectralon, which has a reflectance rate of 99% for the wavelength of 1070 nm. The sphere diameter is 5.3 inch, and it has 6 ports to mount a sample, detector and light source depending on the measurement processes, and there is also an additional port to trap the light reflecting directly from the surface. With the integrating sphere assembly, it is possible to perform reflectance measurements through directional-hemispherical geometry. In the directional-hemispherical geometry measurement method, incoming light directly strikes onto a sample and the detector measures hemispherical portion of reflections. Most of the spheres are designed in a way to allow the incoming light to hit onto the surface at a short angle, between 0° and 10° (mostly at 8°), with the surface normal. This angle is chosen, because it is so close to the direct angle (parallel to the surface normal), and on the other hand, it significantly reduces back-reflections to the light source. The design of the integrating sphere is suitable for the measurement of reflectance by $directional/8°$ ($d/8°$) geometry. Furthermore, both the total reflectance and diffuse reflectance can be measured directly with the sphere, but specular reflectance is calculated from this relation: $R_t = R_d + R_s$. Where R_t is the total reflectance; R_d is the diffuse reflectance; and R_s is the specular reflectance. The RTC sphere system includes an Indium Gallium Arsenide detector (IDA-050-U-RTA-CX), which is sensitive at a wavelength range of 800 nm to 1700 nm.

3.1.2. Reflection and Transmission Measurements

The influence of a laser beam on a material depends mainly on the absorption rate of the material. Hence, by using an integrating sphere with an Indium Gallium Arsenide detector system, reflectance and transmittance values of the single-side-polished Czochralski growth p-type Si wafer with (111) orientation were measured in laboratory. Measurements were carried out by using a CW laser source (Thorlabs-S1FC1060) with 1070 nm wavelength. Since the laser emission power is so small (< 25 mW), the surface temperature of the specimen did not change. So, the acquired reflection and transmission values were accurate for room temperature.

By using the RTC sphere (Figure 3.1), the reflectance and transmittance values of Si wafer were measured. Reflectance measurement was performed firstly for the total reflectance (R_T), then for the diffuse reflectance (R_D). Hence, by the relation of $R_T = R_D + R_S$, specular reflectance (R_S) of the specimen was acquired.

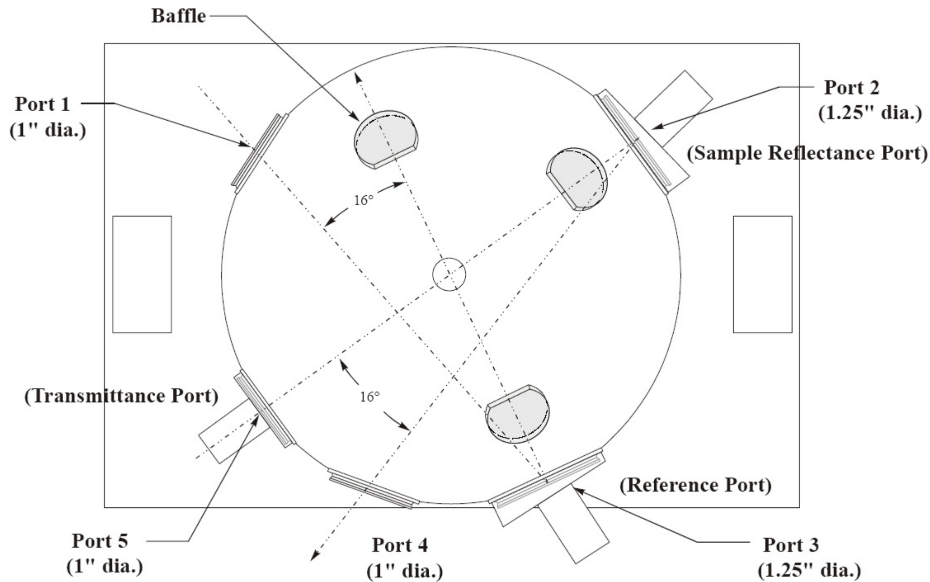

Figure 3.1. Schematic of the RTC sphere used in optical properties measurements ([43]).

Reflectance measurement was carried out as follows: firstly, the dark current was recorded (S_{Dark}) by the detector, then the reflectance standard was located in the sample port (Port 2 in Figure 3.1) and was enlightened by 1070 nm laser beam, then the detector value was recorded ($S_{Std}(\lambda)$), and finally, the sample was replaced by the reflectance standard and under illumination of a laser beam, the value of the detector was recorded ($S_S(\lambda)$). Then, the reflection of the sample was calculated as:

$$R(\lambda) = R_{Std}(\lambda) * \frac{S_S(\lambda) - S_{Dark}}{S_{Std}(\lambda) - S_{Dark}} \tag{3.1}$$

Where $R_{Std}(\lambda)$ is the reflectance of the standard sample for the specified wavelength (λ).

Moreover, transmittance of the Si wafer was also measured through the integrating sphere in the same way. In this case, the (111) Si sample was placed into the transmittance port (Port 5) and the reflectance standard sample was placed in Port 2. Firstly, the dark noise was recorded (S_{Dark}), and by illuminating the sphere with laser beam, the detector value was recorded ($S_{Ref}(\lambda)$), and the Si sample was settled in the port where the laser enters into the sphere, and the detector value was recorded ($S_S(\lambda)$). Finally, the transmittance of the sample was calculated by the formula:

$$T(\lambda) = \frac{S_S(\lambda) - S_{Dark}}{S_{Ref}(\lambda) - S_{Dark}} \tag{3.2}$$

As a result, (111) p-type Si wafer reflectance and transmittance were measured as $R(\lambda) = 40\% \pm 1\%$ and $T(\lambda) = 39\% \pm 1\%$ respectively. Besides, the specular reflectance ($R_s(\lambda)$) is $90\% \pm 2\%$ and diffuse reflectance ($R_d(\lambda)$) is $10\% \pm 3\%$ for Si wafer. Hence, the absorbance of the Si sample can be found by the relation:

$$A(\lambda) = 1 - R(\lambda) - T(\lambda) \tag{3.3}$$

So, the absorbance of the sample is $21\% \pm 1\%$ for 1070 nm wavelength.

3.1.3. Optical characterization of Si wafer

Besides the absorbance, reflectance and transmittance values can be used in calculation of the absorption coefficient, the refractive index, the extinction coefficient and the dielectric constants of the materials. In this section, these parameters will be extracted from the measured reflectance and transmittance values of Si wafers.

Initially, absorption coefficient (α) is determined by the relation ([23]):

$$\alpha = -\frac{1}{t} ln \left(\frac{C - R^2 + 2R + T^2 - 1}{2T} \right) \tag{3.4}$$

$$C = \sqrt{(R^2 - 2R - T^2 - 1)^2 - 4(2 - R)R} \tag{3.5}$$

In the equation of the α, C is an abbreviation of a value defined in the second line. According to the calculations, the absorption coefficient is 5.4 $\mathrm{cm}^{-1} \pm 0.7$ cm^{-1}. From absorption coefficient, the value of the extinction coefficient (k) is calculated as $4.6 * 10^{-5} \pm 0.5 * 10^{-5}$ by the relation:

$$k = \frac{\alpha * \lambda}{4 * \pi} \tag{3.6}$$

Furthermore, the refractive index (n) of the sample can be found by the Fresnel equations for normal angle incident beams. Since the reflectance and transmittance measurements were held at the angle of 8°, the Fresnel relation may be simplified for normal incidence. Hence, the relation becomes:

$$R = \left(\frac{n-1}{n+1}\right)^2 \tag{3.7}$$

The refractive index for p-type Si sample is found as 4.43 ± 0.07.

Finally, dielectric constants of single-side-polished Boron doped (111) Si wafer is acquired by the formulae:

$$\epsilon_1 = n^2 - k^2; \quad \epsilon_2 = 2 * n * k; \quad \epsilon = \epsilon_1 + i * \epsilon_2; \tag{3.8}$$

and the result is:

$$\epsilon = 19.6 + i * 4.07 * 10^{-4}. \tag{3.9}$$

3.2. Gaussian Beam Experiments in Different Media

3.2.1. Sample

In this study, p-type (doped with Boron) Si (111) wafers with a thickness of 510 μm $\pm 5\mu m$ were used. Initially, the Czochralski growth wafers were cut into small pieces with a diamond cutter then cleaned by standard cleaning procedure with an ultrasonic cleaner. The samples were put in acetone, ethyl alcohol and deionized water for 20 minutes respectively, and this is procedure should follow this order. The sheet resistance of the small pieces is 15 Ω/sq as per the manufacturer's specification.

Furthermore, the Phosphorous doped (n-type) Si wafer with (100) wafer orientation was used in CW laser-matter interaction experiments.

3.2.2. Laser Sources

In the surface manufacturing studies, two kinds of near infrared laser source were used. One of them was an electro-optic Q-switch laser system (EKSPLA NL230) which produces nanosecond laser pulses. There is Nd:YAG rod in the laser system. Diode pumped generated laser beam wavelength is 1070 nm at first harmonic generation. A single pulse laser duration is 5.5 ns with 0.2 ns optical pulse jitter, and the repetition rate is 100 Hz with a frequency divider system included in the laser control unit. There are two types of operation mode: adjustment and maximum modes. The energy of single pulse differs from 0.06 mJ up to 80 mJ thanks to the Q-switch delay in adjustment mode. Pulse energy of a single pulse is 91 mJ at maximum operation mode (Figure 3.2). The pulse energy stability for maximum energy is 0.27 % at maximum mode. Polarization of the laser beam is horizontal. The beam profile is "Top Hat" in the near field and "Gaussian-like" in the far field. Beam diameter is 4.5 mm. Beam divergence is less than 0.8 mrad. Beam propagation ratio (M^2) is less than 2.5. Peak power of the laser pulse is 16.4 MW for a collimated beam with 4.5 mm beam diameter at 1070 nm wavelength. While the power density of the laser source is 58.5 W/cm^2, the energy density is 0.58 J/cm^2. Finally, the average power of the nanosecond pulse

laser is 9.3 W. On the other hand, there is a batch mode which operates in single- or multi-pulse mode.

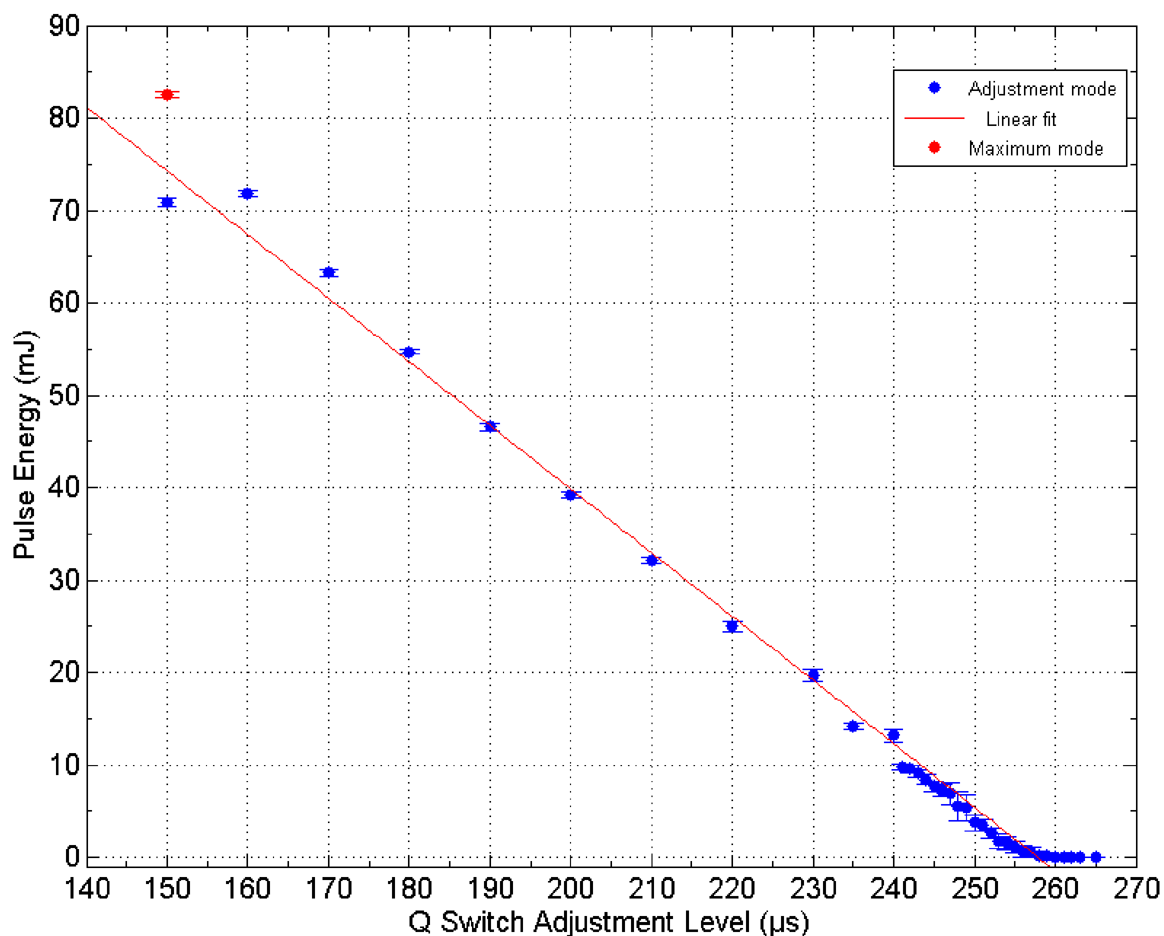

Figure 3.2. Pulse laser energy versus Q-switch delay and linear fit [measured by a pyroelectric energy meter (Ophir PE50-DIF-C)].

The second near infrared laser source was a continuous wavelength (CW) Ytterbium fiber laser. The CW laser is an IPG product named YLR-100-WC. Maximum emission wavelength of the laser source is 100 W for 1070 nm wavelength. Its emission power can be tuned from 0.4 W to 100 W. Beam propagation ratio (M^2) is 1.04. Beam shape is Gaussian with single mode laser beam. $1/e^2$ value of the collimated beam diameter is 6.8 mm with a divergence angle of 135.5 mrad.

3.2.3. Analysis of Gaussian Beam

3.2.3.1. Theoretical Calculations. The focused beam size depends on the incoming light width and its beam shape as well as the lens properties. Since the sample is located in the far field, the incoming beam shape is nearly Gaussian. The ns pulse laser beam spot diameter is 4.5 mm, which also equals to the size of the beam just before the optical lens. A fused silica plano-convex lens with 200 mm focal length was used in the experiments while the sample was located in the Rayleigh range of the beam after the fused silica lens. Hence, on the sample surface, beam diameter equals to the beam waist size. As mentioned in Section 2.4.1.1, the ns pulse laser beam spot size was calculated. Then, theoretically, beam diameter was 156 μm on the sample surface. Figure 3.3 demonstrates the 2-D and 3-D graphs of a Gaussian beam spot with 156 μm diameter. The intensity was normalized in the graphs which is drawn in MATLAB.

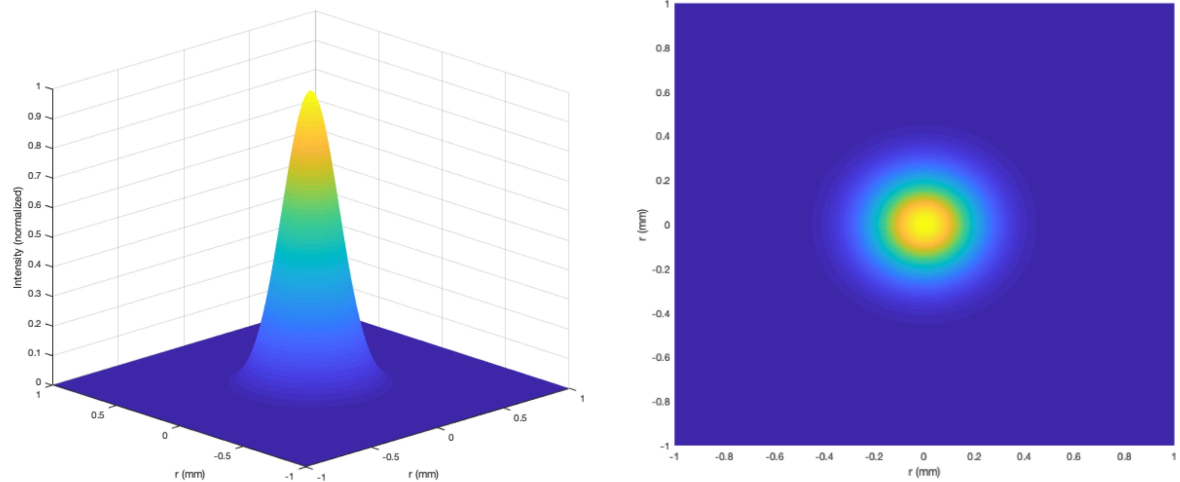

Figure 3.3. A Gaussian beam distribution with 156 μm beam spot and normalized beam intensity in 3-D and 2-D views.

3.2.3.2. ZEMAX-EE Calculations. By using the ZEMAX optical design program in sequential mode, the laser beam spot size can be determined. The parameters used in the simulation are given in Table 3.1. Firstly, the experimental setup is designed

in the software by using the lens catalog containing so many optical materials (lenses, mirrors, beam splitters, etc.). Also, the ns pulsed laser source is defined in the laser properties section by defining its beam waist and M^2 values. Then the beam radius is calculated for different conditions including air, water and glycerin. Main ambient is air in ZEMAX, that's why one should define the other ambient conditions by indicating refractive index (N_x), Abbe number (V_d) and deviation of the partial dispersion (ΔP_{gF}). The values for water and glycerin are shown in Table 3.2. Since only the fundamental mode of the laser cavity (1064 nm) is used in the experiments, the deviation of partial dispersion is 0.0 for all ambient conditions.

Table 3.1. ZEMAX Optical Design Program Lens Data Editor Parameters

No.	**Comment**	**Curvature**	**Thickness**	**Glass**	**Tilt-X**
Obj	Laser Source	0.0E+00	1.00E+10		0.0E+00
1	dummy	0.0E+00	5.00E+02		0.0E+00
2	Coord. Break	0.0E+00	0.0E+00		4.5E+01
3	33-079 Edmund O.	0.0E+00	0.00E+00	MIRROR	0.0E+00
4	Coord. Break	0.0E+00	-2.5E+01		4.5E+01
5	LA4984 - Thorlabs	1.09E-02	6.57E+10	F-SILICA	0.0E+00
6	Liquid Media	0.0E+00	2.00E+02		0.0E+00
7	Si Wafer	0.0E+00	0.00E+00		0.0E+00
Ima	Image	0.0E+00	0.0E+00		0.0E+00

Table 3.2. Water and Glycerin material properties used as inputs in the ZEMAX.

	Water	**Glycerin**
N_x	1.3262	1.4631
V_d	55.7944	54.6
ΔP_{qF}	0.0	0.0

After paraxial Gaussian beam analysis, according to the input parameters defined above, beam spot sizes are 103.6 μm in air and 103.07 μm in water and 103.06 μm in

glycerin. Laser beam spot size in liquid environment is smaller than the one in the ambient conditions since the water and glycerin have denser medium than the air. In another words, the refractive indexes of liquids are bigger than the air index, thereby yielding the self-focusing effect. However, the change in spot sizes is minor, because the thickness of the liquid above the sample is so small (2 mm) in comparison to the focal distance of the lens (200 mm).

3.2.3.3. Beam Monitoring. Near IR nanosecond pulse laser beam was profiled and measured through the scanning slit optical beam profiler (Thorlabs - BP209-IR). Using scanning-slits technique, pulse beam profile was monitored before the fused silica lens but also in the far field region. On the other hand, since the beam is pulsed, the measuring was done in toggle mode which collects the sequential measurements in a single image. Beam size was determined by the $1/e^2$ value of the Gaussian filtered data as can be seen in Figure 3.4. Furthermore, 3-Dimensional (3-D) illustration of the near IR pulse laser beam was performed as shown in Figure 3.5.

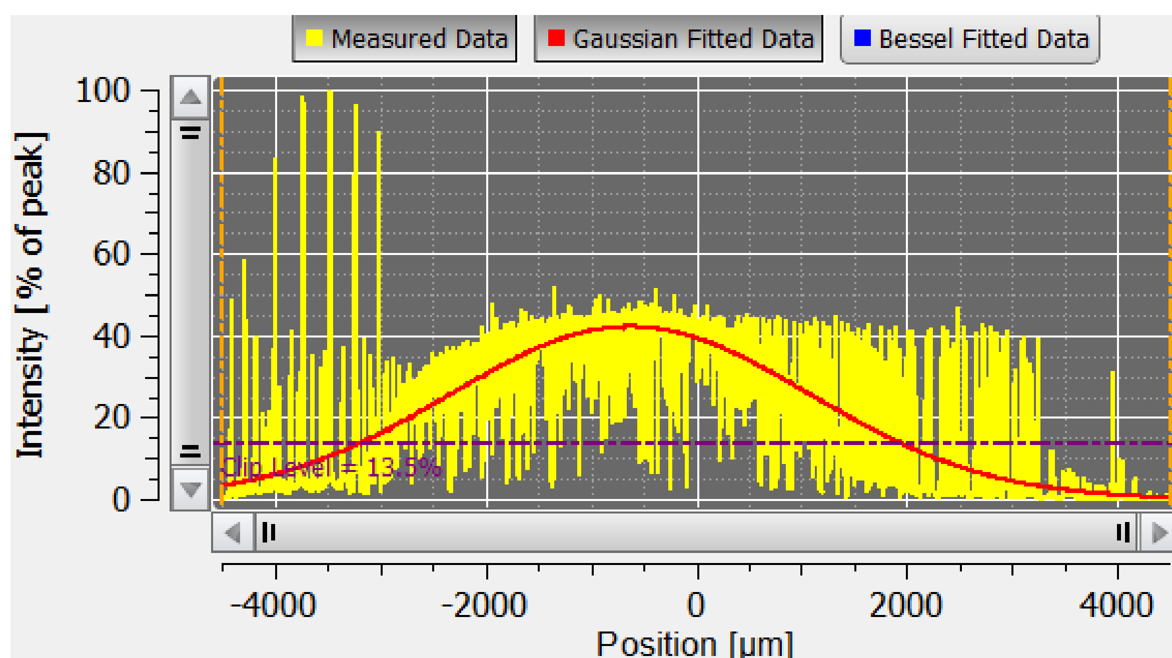

Figure 3.4. Nanosecond pulse laser beam horizontal profile in far field region.

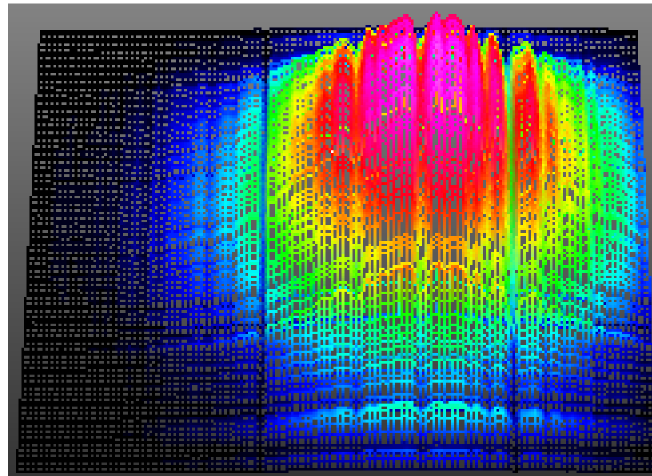

Figure 3.5. 3-Dimensional nanosecond pulse laser beam shape in far field region.

3.2.4. Experiments in Different Media

Experimental setup is shown in Figure 3.6. The experiments were conducted in the far field. The optical YAG mirror (Edmund optics 33-076) was used to propagate the laser beam perpendicularly before focusing the beam on the sample surface with a plano-convex lens (Thorlabs LA4984). The plano-convex lens is made of fuse silica and its focal length is 200 mm. It was mounted on the sample in a stabilized manner, and during the experiments the position of the lens was not changed. Prepared Si samples were located at the focal position of the lens on a translation stage which can move in two lateral directions, namely x- and y- direction. The experiment set-up was located in ISO 8 class (100000 class) clean room at TÜBİTAK BİLGEM. The temperature was stabilized at 18°C and humidity was 50 % in the clean room. After the experiments were completed, 3-D surface and topography analysis of laser induced damage areas was performed by an Optical Microscope (Bruker ContourGT-K), an AFM (Nanosurf NaioAFM) and a SEM (JEOL JSM 6335F).

3.2.4.1. Interaction in Ambient Medium. As noted above, laser-material interaction depends both on laser characteristics and sample properties. In ambient conditions, both the laser source and the Si specimen were changed during the experiments. While

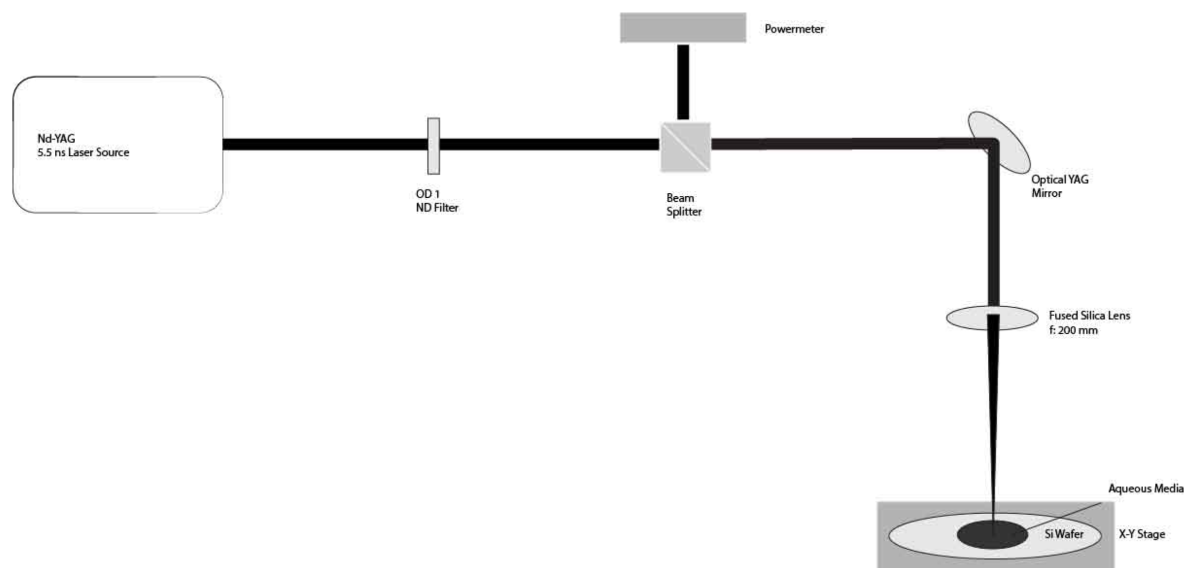

Figure 3.6. Experimental setup in Gaussian beam experiments.

the laser wavelength was constant at 1070 nm, the modes of the laser sources were used in two different types including a CW laser and a ns pulse laser. On the other hand, in CW laser studies, Si wafers which have different orientation and doping type were studied and examined.

Continuous Wavelength Laser Studies at 1070 nm. (100) n-type and (111) p-type Si wafers were illuminated by nearly same CW laser average power at different time lengths. As the sample was being illuminated by the NIR CW laser beam, on the other hand, the temperature of the surface was measured by non-contact measuring technique by a long wavelength infrared (LWIR) thermal camera (FLIR T450sc). In thermal measurements, the important point is that the specimen's emissivity value must be known in order to be sure of the correctness of the measured temperature data. The emissivity value of the Si wafer is acquired from [44] based on the temperature ranges. In measurements, Si wafer emissivity was taken as 0.60 from 25°C to 450°C and 0.70 from 500°C to 1200°C. While the CW laser beam was focused onto the specimen's surface, the laser source emission power was 85 W and the focal spot size was 30 μm, so the beam irradiance on the surface was approximately 30 kW/cm^2. Hence, the p type

Si wafer with (111) orientation was illuminated by a CW laser beam for 10 seconds, and the heating and cooling of the specimen surface can be seen in Figure 3.7.

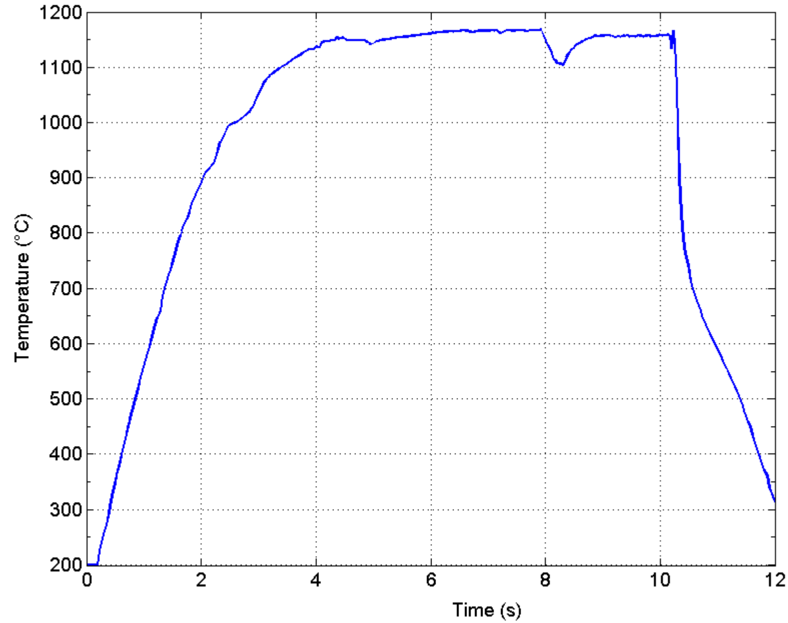

Figure 3.7. Temperature graph of p-type (111) Si wafer under illumination of 30 kW/cm^2 laser irradiance for 10 s. The temperature measurement was taken by LWIR thermal camera.

In CW laser Si interaction mechanism, the first stage is slip formation in wafer [34] before the ablation occurs. Near the laser damage threshold energies of Si wafers, surface cracks and melted zones differ in detail based on orientations and doping types.

For analysis, the NIR CW laser parameters were changed in terms of laser output power, beam spot size and operation duration. The ablations in both p-type(111) and n-type(100) Si materials were observed based on variations of the laser characteristics. Mechanically, after the radiation of a CW laser beam, similar damage regions occur in different Si wafers. The ablated structure can be classified, from the center to the outer, as a fully melted region, partially melted region and crack manufacturing in both types of Si. Moreover, although the ablation zones show similar behaviors in two specimens, through deep analysis, one can easily understand that, as regards to the Si sample

properties (the doping type and the wafer orientation), intrinsic differences emerge in damage areas. Optical Microscope (OM) images in Figure 3.8 and Figure 3.9 show (100) n-type Si wafer and (111) p-type Si wafer ablation zones respectively. On the one hand, two samples damage areas can be classified with three main regions: melted zone, partially melted zone and crack production. On the other hand, specifically, in regions of partial melting and crack orientation, n-type and p-type samples are really different from each other. In (100) n type Si sample, the angle between two cracks is approximately 90°. But in case of (111) p-type Si wafer, the angle of the cracks is 60° (Figure 3.10). Furthermore, partially melted zones also differ from each other in terms of structural deformations. In Phosphorous doped (100) Si wafer, the partially melted zone includes line distributions like the cracks itself, because the cracks cause multiple reflections on the surface and increase the surface absorption [33]. For instance, in Figure 3.11, at a low irradiance, the center of the laser beam causes semi-melting at the center and some crack formation around the center. However, in Boron doped Si wafer with (111) orientation, the partial melting case is a completely different phenomenon. The crack-based partial melting cannot be resolved in Optical Microscope images in p-type (111) Si wafer.

According to the temperature data obtained, even though the p-type Si wafer surface under laser illumination cannot reach the value of the melting point of Si (1442°C), OM images demonstrate the occurrence of ablation. The reason for why a complete melting or a partial melting takes place is that NIR CW laser induced damages are thermal based in Si wafer. By increasing the temperature of the structure, thermal stress also increases. Additionally, thermal expansion is restricted to the cooling areas. Finally, the portion with high temperature would slip because of the kinetic energy differences of the atoms. These slip regions can be seen as cracks on the surface, and these cracks cause more reflections as the laser beam continues to fall down. This is the reason why the absorption inside the region increases and the surface melts.

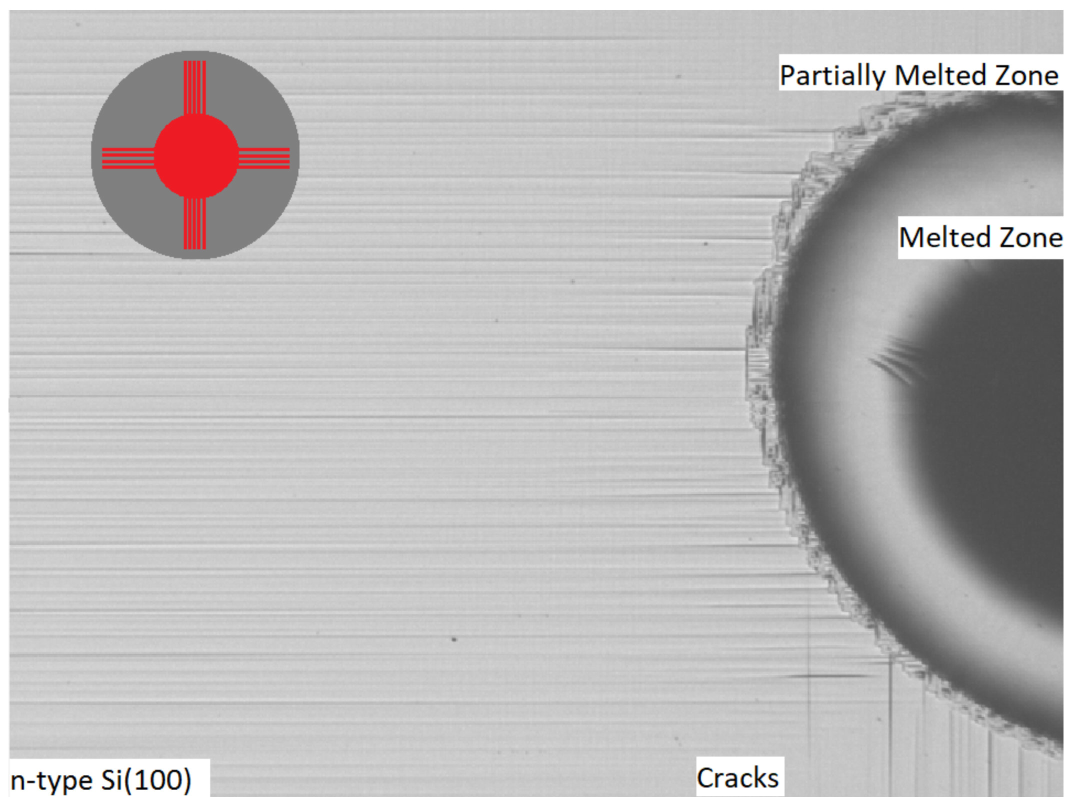

Figure 3.8. OM image of (100) n-type Si wafer surface after CW laser irradiation.

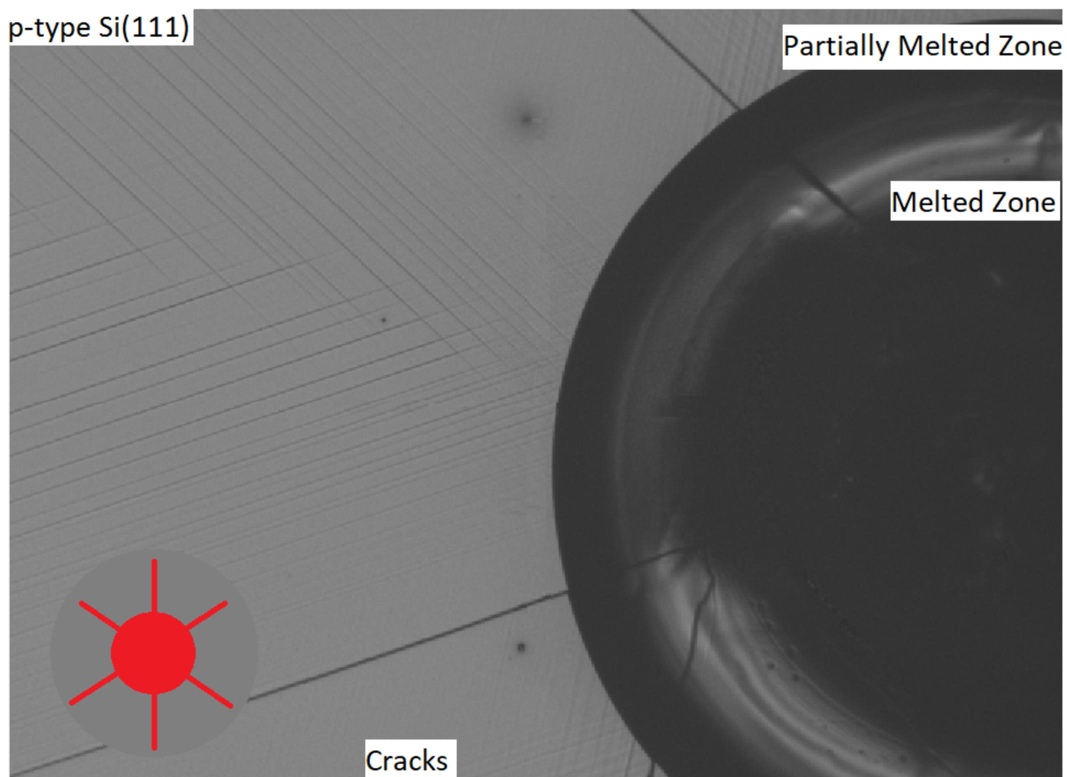

Figure 3.9. OM image of (111) p-type Si wafer surface after CW laser irradiation.

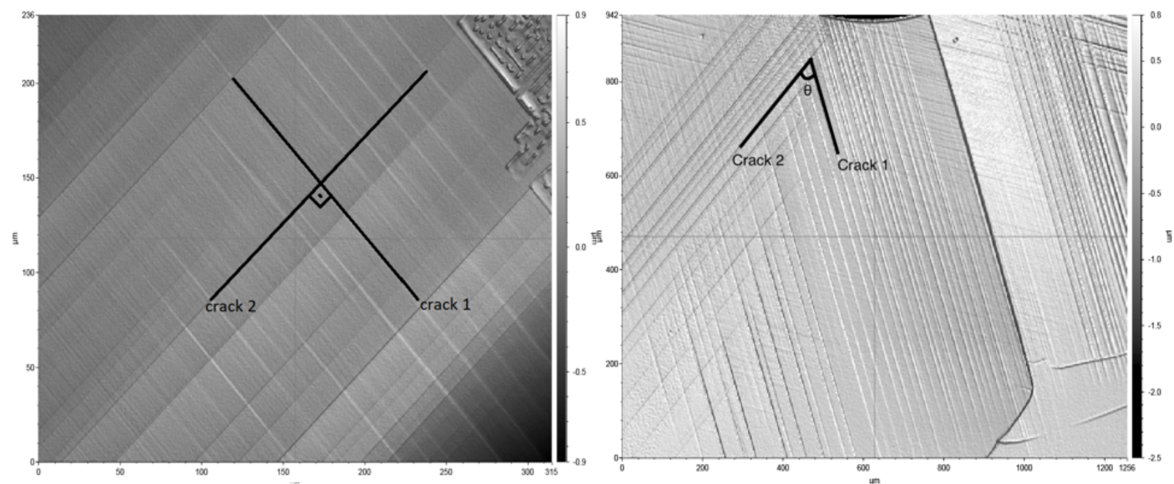

Figure 3.10. The angle between two cracks in n-type (100) (left) and p-type (111) (right) Si wafer after CW laser interaction. In n-type (100), the angle is 90° and in p-type (111) the angle is 60°.

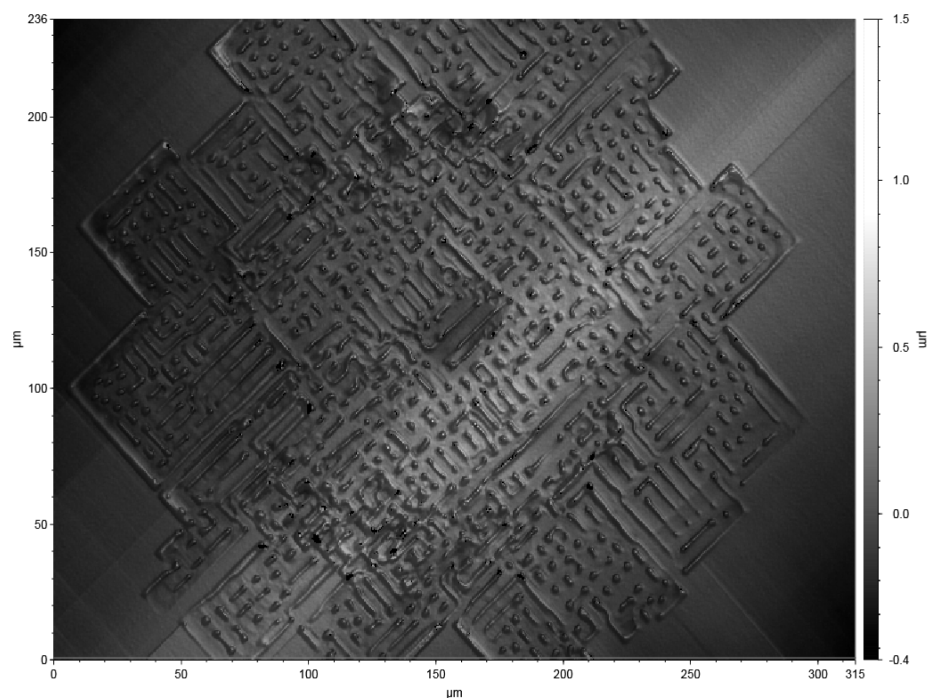

Figure 3.11. Before the ablation process, the partially melted zone in n-type Si wafer (100) after CW laser illumination.

Pulse Laser Studies at 1070 nm. Laser induced material interaction studies continued with NIR ns pulse laser source and with p-type Si (111) sample in clean room experiment conditions as noted above. Firstly, the damage threshold of p-type Si specimen was determined with a single pulse by changing the laser emission energy. The specimen was located at the focal position of the pulse laser beam and the beam waist size at that point was 156 μm theoretically. The laser source energy was increased from minimum value to the maximum by changing the Q-switch adjustment level. The single pulse induced ablation and heat affected zones (HAZ) of Si samples were profiled with OM and SEM. In Figure 3.12, SEM image shows the surface structures after irradiation by a single pulse with 18 mJ laser energy. In figure, inner line shows the ablation crater whose depth is 13.8 μm. The ablated crater does not include any of the residual effects or structural deformations. Moreover, the molten material from the central part was located in the peripheral area (the outer line in the image). While the diameter of the ablation zone is in the order of the laser beam spot size, the HAZ diameter is much bigger than the focal diameter because of thermal expansion. In peripheral zone (HAZ) it can be seen that recoiling features and ripples were formed due to the high peak energy of the single pulse.

By looking at the SEM images of the HAZ produced by higher energies in detail, the ripple structures were observed obviously around the ablation area. For instance, in Figure 3.13, the peripheral area for 50 mJ laser pulse energy includes sub-wavelength ripple formations. According to the results, ripple's length is approximately 50 μm and periodicity of ripples is around 300 nm. On the other hand, based on AFM results, ripples height was found as 86.1 $\pm$ 19.5 nm (Figure 3.14). The self-assembly ripple morphologies are only seen in case of high pulse laser energies, the reason for which may be the stress between borders of the HAZ and the ablation zone. The confinement of molten material is located on this border.

According to the ablation diameter measurements, as the energy of single pulse increases, both the ablation and the HAZ diameters increase linearly, which can be seen in Figure 3.15-a. Moreover, the same tendency can be observed in case of the low rate multi-pulses' illumination upon the Si sample surface (Figure 3.15-b). Even

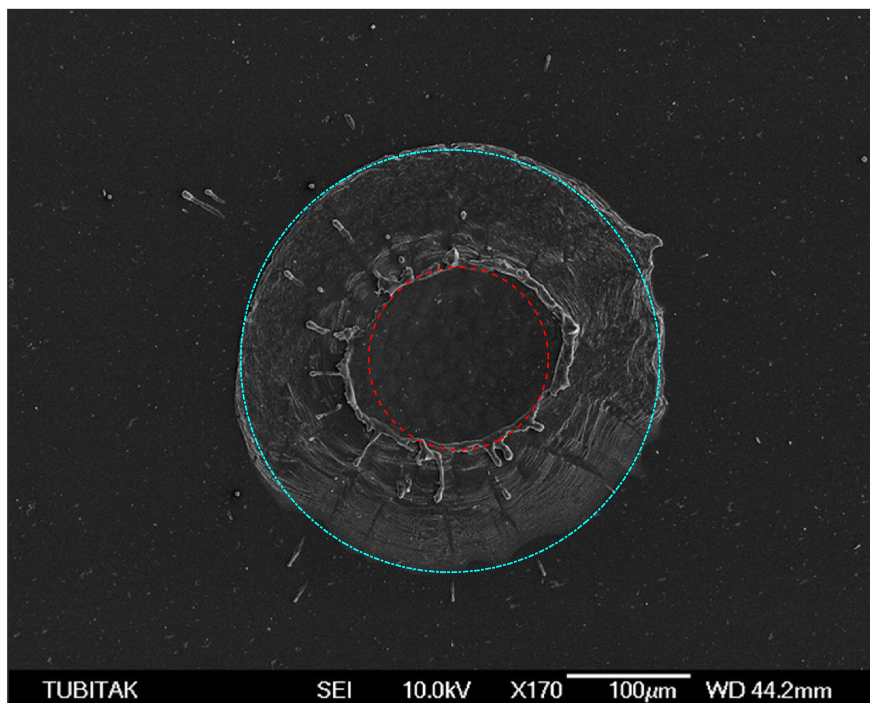

Figure 3.12. SEM image of a damage area after a single pulse interaction (18 mJ energy). Inner ring shows the ablation zone and outer ring shows the HAZ area.

though the number of pulses gets higher until 5 pulses, ablation craters with same size can be formed. OM images of laser induced damage zones in p-type (111) Si wafer with single pulse and multi-pulses can be seen in Figure 3.16

3.2.4.2. Interaction in Liquid Medium. In order to reduce the residual effects of ns pulse laser induced damages on p-type (111) Si wafer, the same experiments were carried out in liquid medium. Firstly, approximately 2400 mm^3 water was placed upon the Si sample in the same experimental setup. After the identical systematic experiments were accomplished, the results were compared to the ambient condition's outputs in terms of the laser induced damage threshold (LIDT) of the Si sample and the morphologies of damage areas. Finally, the tests were repeated for the glycerin medium under same test conditions and with similar procedures. However, these experiments were conducted with low energy densities for determining the LIDT value of p-type (111) Si specimen. Unlike the air medium, the occurrence of peripheral area has reduced in water environment and even completely disappeared in glycerin environment.

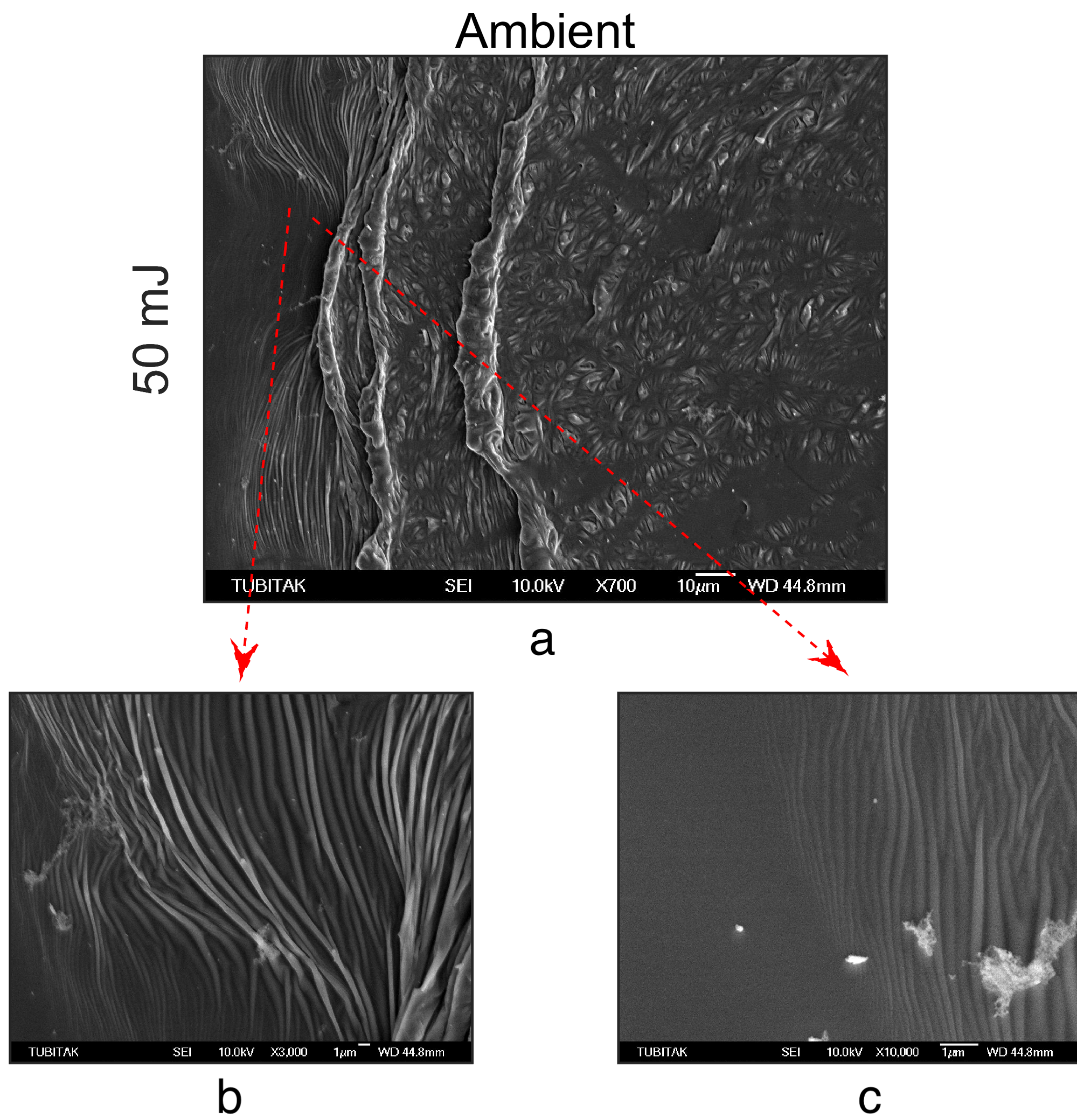

Figure 3.13. SEM image of a ripple zone between ablation and HAZ area. (b) and (c) are zoomed areas from (a). The pulse energy is 50 mJ.

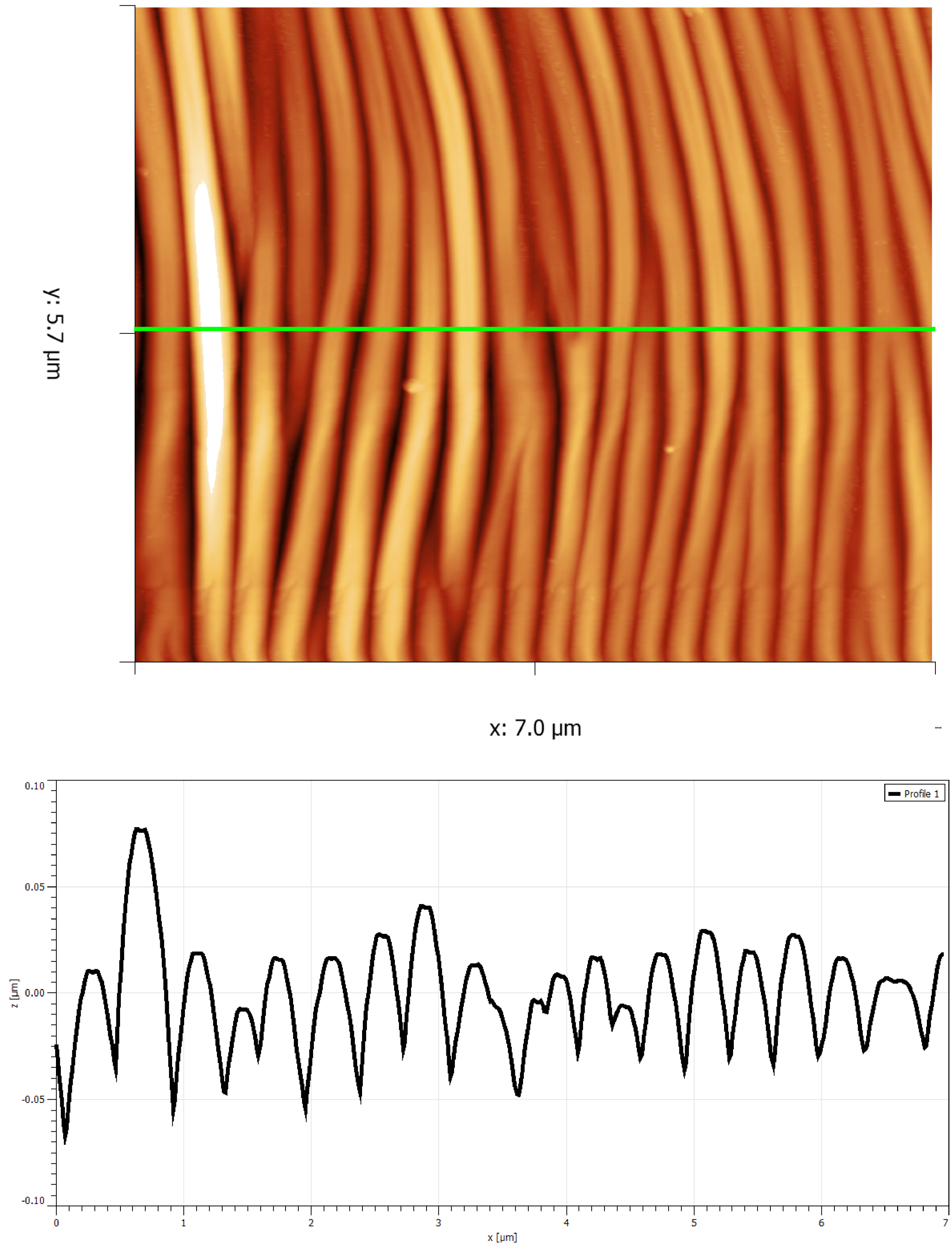

Figure 3.14. AFM topography of self-assembly ripples around ablation zone and HAZ for 50 mJ pulse energy.

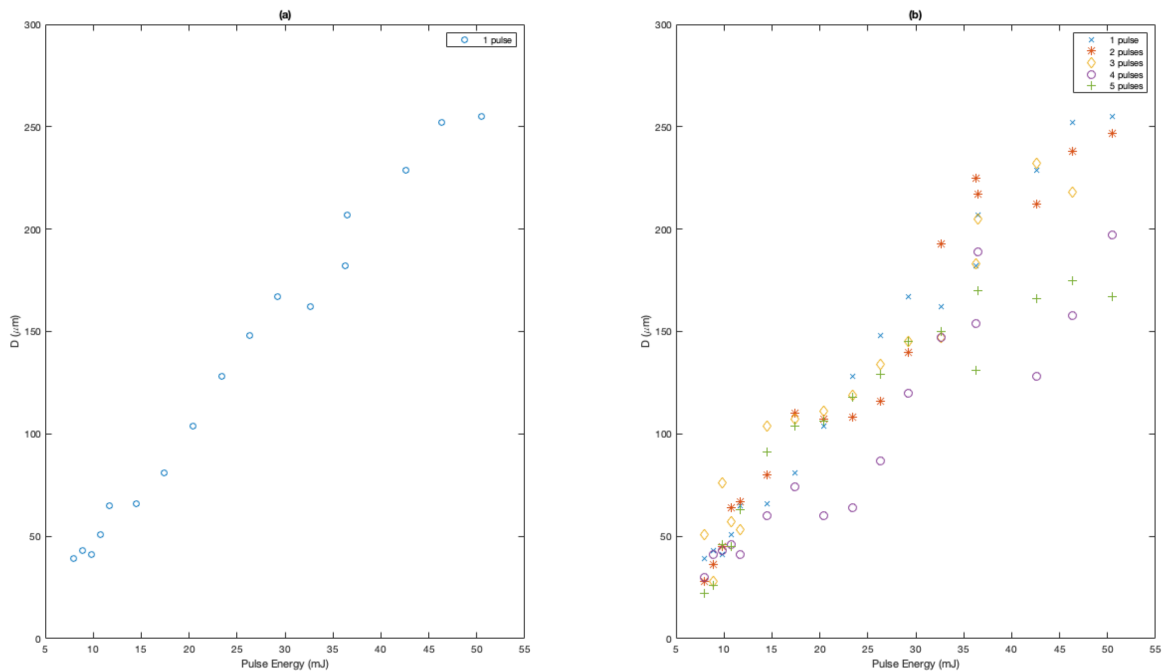

Figure 3.15. Ablation zone diameter values of a p-type (111) Si sample based on the single pulse energy for a single pulse and multi-pulses studies.

SEM images in Figures 3.17 of water and 3.18 of glycerin demonstrate that the ns pulse laser's thermal impacts can be removed completely through a denser medium. Both images were taken from the damaged areas of liquids which were created by the identical single pulse energy (7.9 mJ) and the images have same magnification ratio. As ablation mechanisms are the same in both SEM images, diameters of the damaged areas differ from each other significantly and the residual effects cannot be observed in these studies.

On the other hand, Figure 3.19 shows how the laser pulse fluence affects the diameter of a laser-induced ablation crater. The graphs are drawn for the pulse energy versus the diameter square of the ablation zone. This relationship is used for the calculation of the laser beam spot size and will be explained in the next section.

3.2.4.3. Comparison of the Results. As noted in the introduction of the thesis, the liquid environment in the laser-material interaction process provides more effective cooling to the sample, thereby decreasing the thermal influences in the damage area.

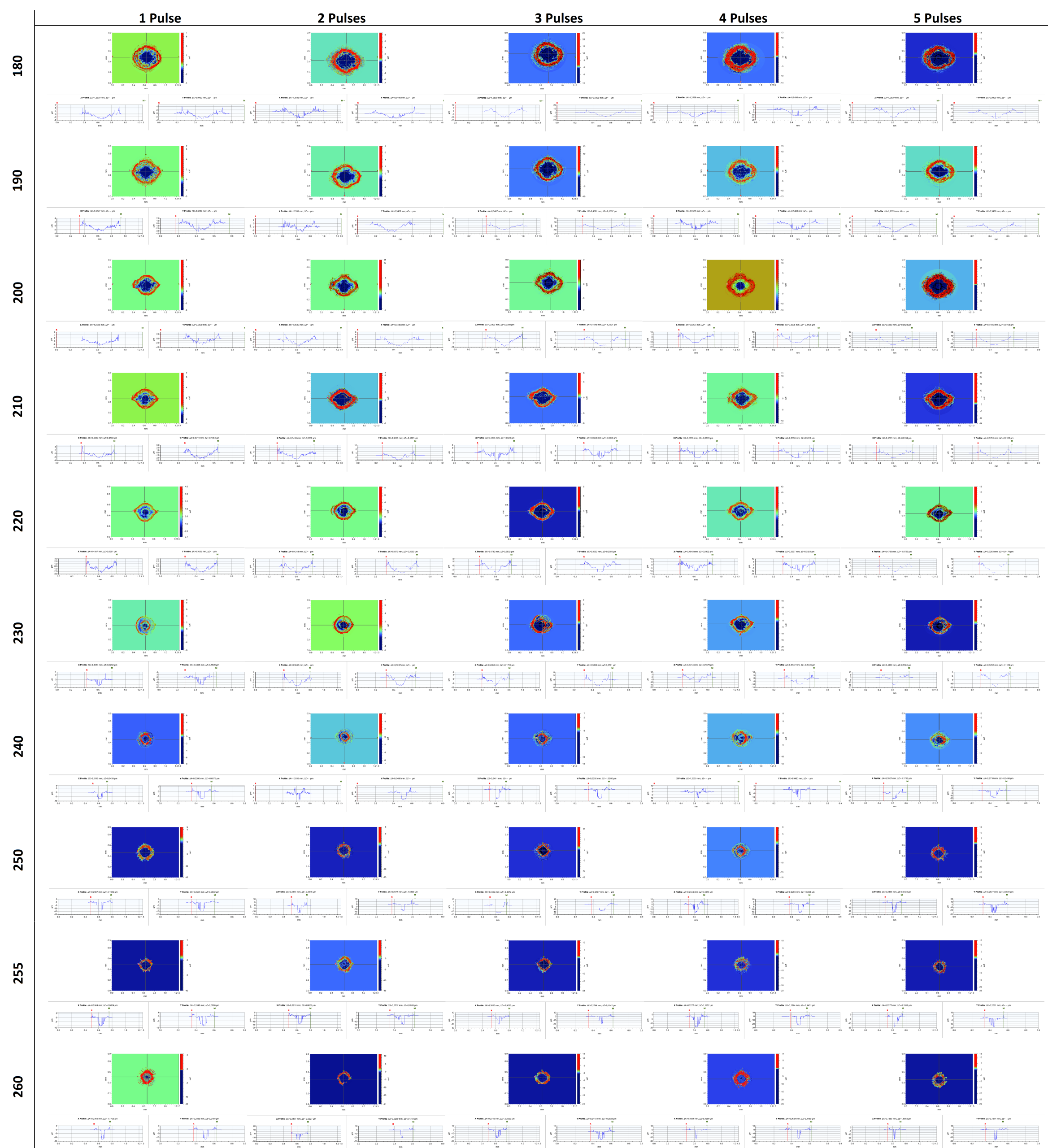

Figure 3.16. OM false color images of laser applied damage areas based on the Q-switch adjustment level and the number of pulses.

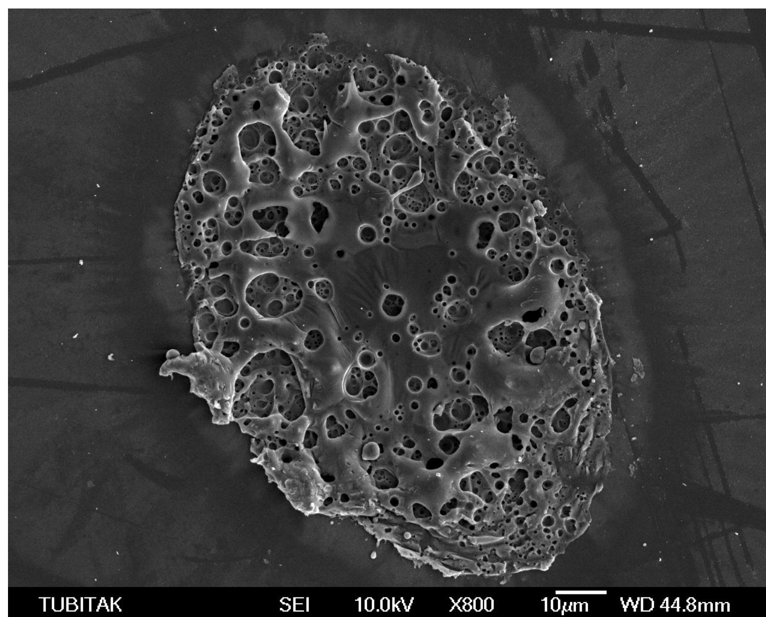

Figure 3.17. Laser induced ablation zone of the Si(111) sample in water environment (SEM image).

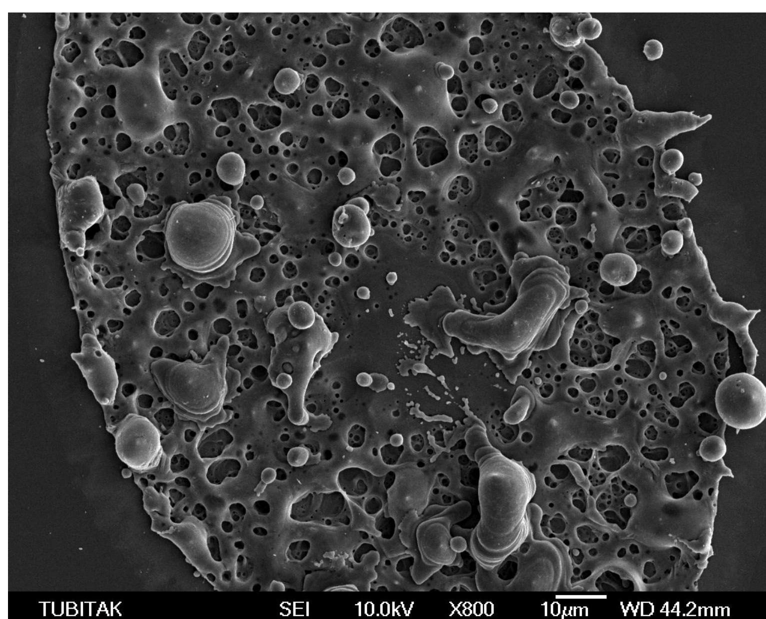

Figure 3.18. Laser induced ablation zone of the Si(111) sample in glycerin environment (SEM image).

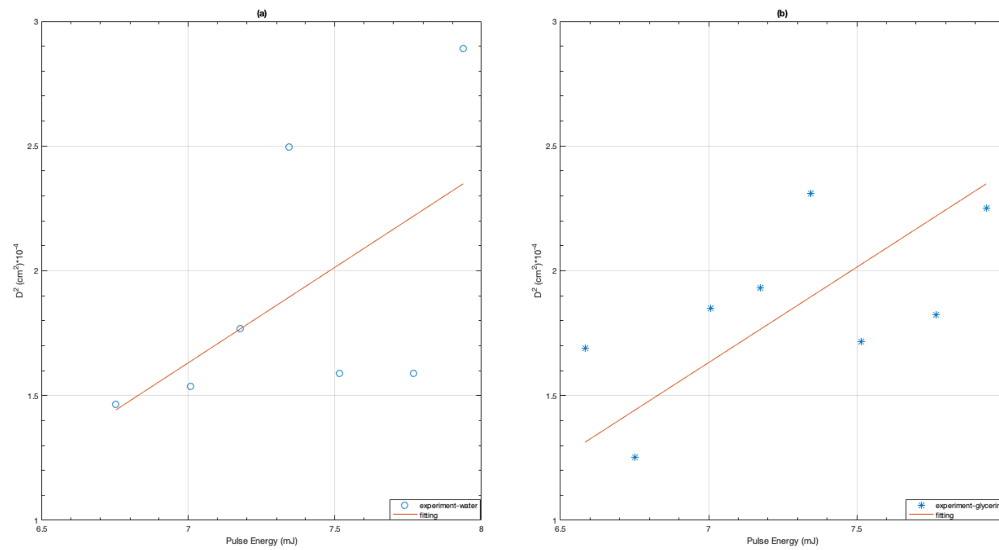

Figure 3.19. The effect of laser pulse energy on diameter square of ablation zones created on the Si(111) in water (a) and glycerin (b) medium.

In this study, NIR ns pulse laser-(111) p-type Si wafer interaction was studied in 3 different environments, namely air, water and glycerin, in order to observe the effects of the medium. Physical properties of the medium with a crystalline Si are given in the Table 3.3.

Table 3.3. Physical properties of Water and Glycerin.

Properties	**Air**	**Water**	**Glycerin**	**Silicon**
Refractive Index(n)	1	1.33	1.46	3.55 (1070 nm)
Thermal Conductivity(W/m.K)	10^{-3}	0.609	0.285	149
Viscosity(Pa.s)	10^{-6}	10^{-3}	0.95	10^{-3}(molten)
Density(g/cm^3)	10^{-3}	1	1.26	2.33
Color	NA	NA	NA	dark gray

In Figure 3.20, the laser-induced regions of Si wafer are shown for various pulse energies and different environments. In a similar way, regardless of the media type, as

ns pulse laser energy decreases, the dimension of damage areas also reduces. In water conditions, the structures like the HAZ formation, redeposition of the molten material and the debris formation, which mostly originate from thermal effects, are decreased significantly. Furthermore, due to the smaller thermal conductivity of glycerin, the ablation zones do not include HAZ in the laser induced area. Hence, the ablation zones are as small as the pulse laser spot size. Additionally, some bubble and cavity formations on the ablation zone can be seen in liquid environments due to the heating of the liquid and the extraction of the molten material from the sample surface.

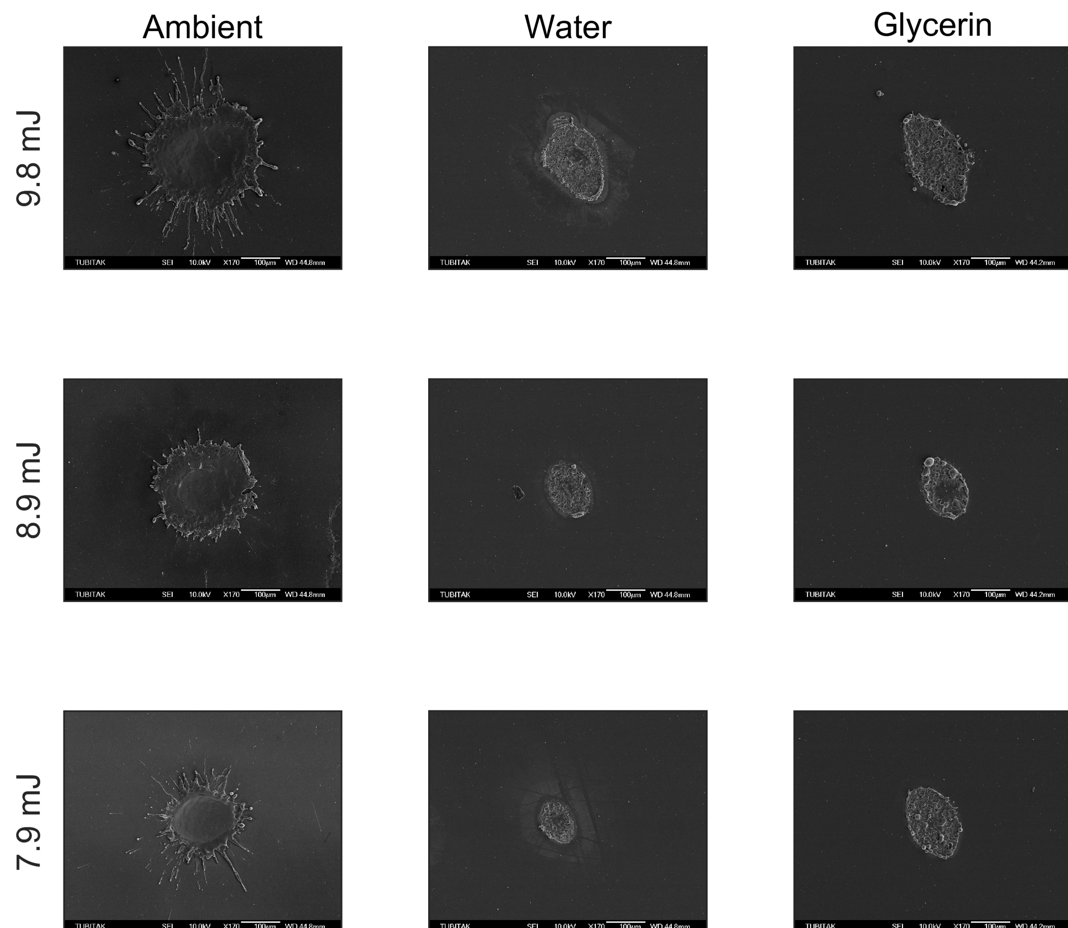

Figure 3.20. SEM images of the ablation zones for different single pulse energies and different media.

When the laser beam profile is Gaussian, the square of the ablation diameter is proportional to the natural logarithm of laser pulse fluence in ultrafast laser ablation (picosecond, femtosecond pulses). In the nanosecond regime laser ablation studies, due to the thermal effects of a laser source, the diameter analysis should be done differently. However, in liquid environment it is possible to assume the focal diameter from the relation between natural logarithm of the laser pulse fluence and the ablation diameter's square. The relation can be shown as [38]:

$$D^2 = 8{\omega_0}^2[ln(F_0) - ln(F_{TH})] \tag{3.10}$$

where D is the ablation diameter, ω_0 is the beam spot size, and F_0 is the maximum laser fluence and F_{th} is the ablation threshold. In water and glycerin environments, the beam radii were calculated from this equation as 83.6 μm for water and 58.9 μm for glycerin. Hence, under illumination of the single pulse laser beam, the LIDT values of p-type Si wafer were obtained as 47.7 and 52.2 J/cm^2 for water and glycerin environments respectively. Therefore, the calculated beam spot size in water deviates from the ZEMAX solution up to 60% and the deviation in glycerin is about 10%. Since there are still low thermal effects in water environment, the deviation of the spot size is a little bit high. However, the important point is that they are in the same order with the theoretical results.

Before the experiments, the average roughness of Si specimens was measured as 0.2 nm with an AFM in the tapping mode. After the Si sample illumination with the ns laser pulses in different media, the depth of the ablated zones was measured. As it can be seen in Figure 3.21, the ablation depth in liquid environment is 2.5 μm regardless of the liquid's type. Yet, in the air medium, a single pulse leads to ablation cracks at approximately 13 μm depth. Hence, the liquid medium provides more controlled ablation structures in the p-type (111) Si wafer by a NIR ns pulse induction.

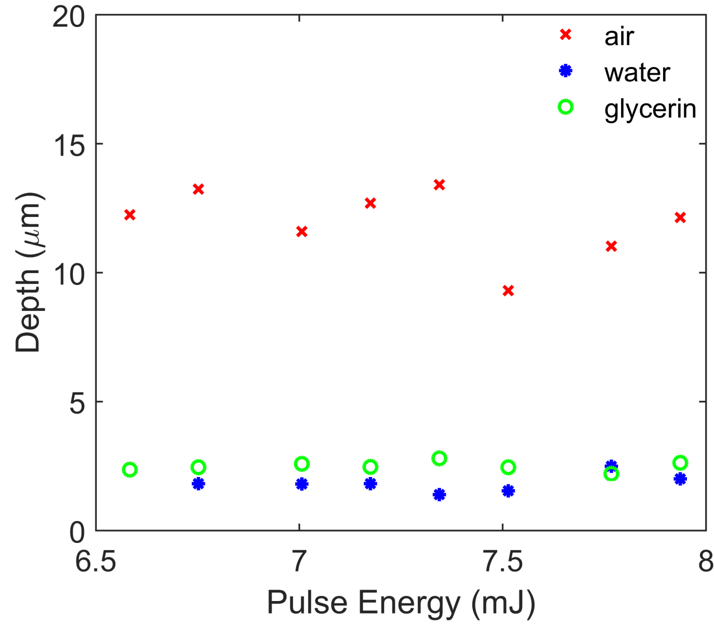

Figure 3.21. Ablation depth of Si samples depending on the laser pulse energy and the medium type.

3.3. Bessel Beam Experiments

3.3.1. Sample

In the laser induced Si wafer interaction studies, the Czochralski growth p-type Si(111) wafers were used for the Bessel beam experiments. The thickness of the specimens is 510 μm $\pm$ 5 μm and the sheet resistance of them is 15 Ω/sq. The Si wafer were cut into small pieces by a diamond cutter before a cleaning process with acetone, ethyl alcohol and deionized water respectively. Then, the prepared sample was placed into the experimental setup.

3.3.2. Laser Sources

For material surface ablation, NIR ns pulse laser source (EKSPLA NL230), explained in Section (3.2.2), was also used in Bessel beam studies. The energy range of the laser source is 0.06 mJ to 90 mJ, and its wavelength is 1070 nm at first harmonic generator. The pulse duration is 5.5 ns, and the beam diameter is 4.5 mm. The beam

shape is "Top Hat" in the near field and "Gaussian-like" in the far field.

For a Bessel beam monitoring, a commercial CW HeNe laser source was used. The wavelength of the HeNe is 633 nm, and its power is smaller than 500 mW. Furthermore, a low power (< 25 mW) 1070 nm CW laser source is also used to image the Bessel beams.

3.3.3. Analysis of Bessel Beam

3.3.3.1. Theoretical Calculations. Bessel beam can be created through different methods, but several types of axicons were used in these experiments. As noted in Section 2.4.2, a first-degree Bessel beam interaction with the Si sample was observed throughout this study. To analyze a Bessel beam, one must know the wavelength and diameter of the incoming beam and the base angle of the axicon lens. In our case, the wavelength in material interaction process is 1070 nm, and the diameter of the Gaussian-like beam is 4.5 mm. There are 2 kinds of axicon lenses with different base angles: 1° and 20°. Figure 3.22 represents the Bessel beam propagation in radial direction depending on the axicon angles. The left diagram is a Bessel distribution for 1° axicon, and the right figure shows the distribution of 20° axicon lens.

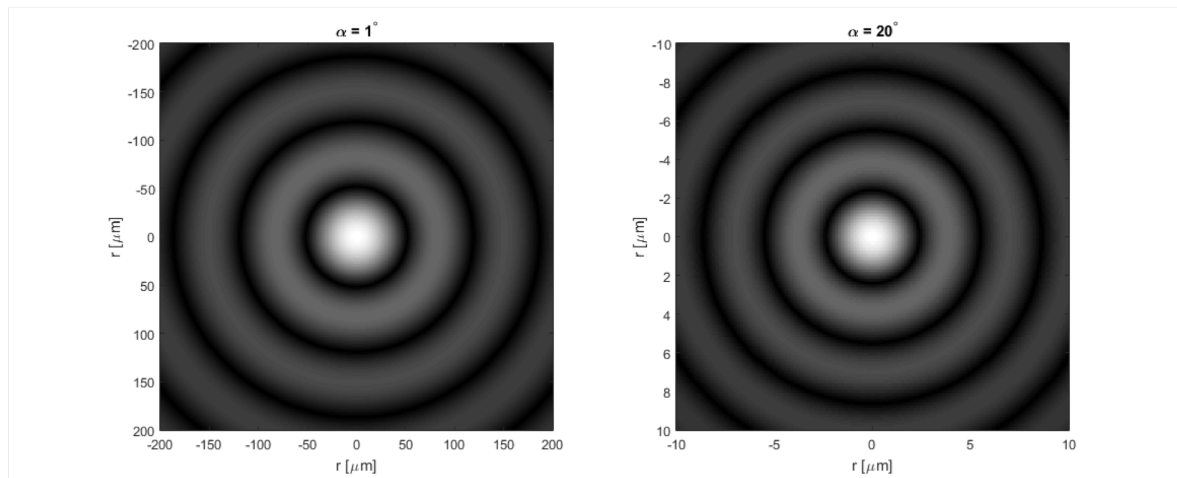

Figure 3.22. Bessel beam profiles in radial direction for different physical angles (left is 1° and right is 20°).

At a constant wavelength, Bessel beam differs in terms of diameter and the Bessel zone lengths depending on the physical angle of the axicon. In Figure 3.23, the image on the right shows the spatial distribution of the intensity of a Bessel beam produced by 1° axicon. From that distribution, the Bessel zone (the graph in the middle) and the radial profile (the graph on the left) of the maximum intensity position can be extracted simply. In consideration of these graphs, 1° axicon lens produces a central point with 103.46 μm diameter at 143.4 mm after the lens, and its Bessel zone is approximately 400 mm. With 20° axicon lens, on the other hand, the diameter of the center is 4.8 μm, the maximum intensity occurs at the position 7.2 mm after the axicon, and the length of the Bessel zone is just 20 mm.

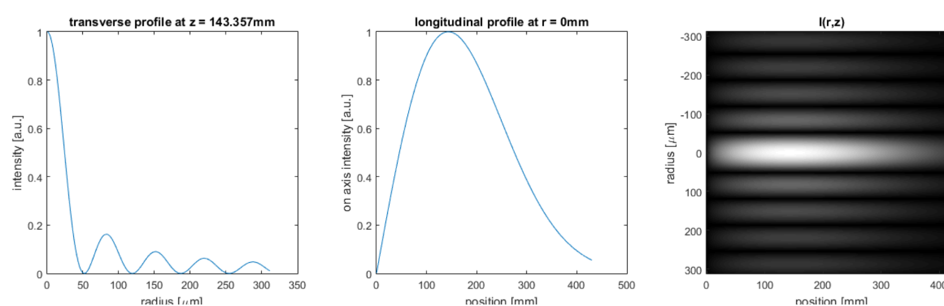

Figure 3.23. Transverse, longitudinal and spatial intensity graphs of Bessel beam after 1° axicon lens for 1070 nm wavelength.

3.3.3.2. ZEMAX Calculations. Bessel beam profile analysis was carried out with ZEMAX-EE optical design program in the sequential mode. The pulse laser parameters were entered as an input to the simulation. After the axicon lens was defined in the lens data editor platform, the Bessel beam profile analysis was completed. By using the through-focus analysis in ZEMAX, longitudinal profiles for different axicon lenses can be acquired as can be seen in Figures 3.24 and 3.25. These figures verify the theoretical values of Bessel zone's lengths and the maximum intensity positions for both axicon lenses. In the images, the beam's profiles are listed after the axicon lens, and the 0 position means the maximum intensity position in simulation. 0 position is 143 mm after the 1° axicon in Figure 3.24 and 7 mm after the 20° axicon lens in Figure 3.25.

Moreover, Figure 3.26 shows a radial profile of a Bessel beam produced by a 20° angle axicon lens.

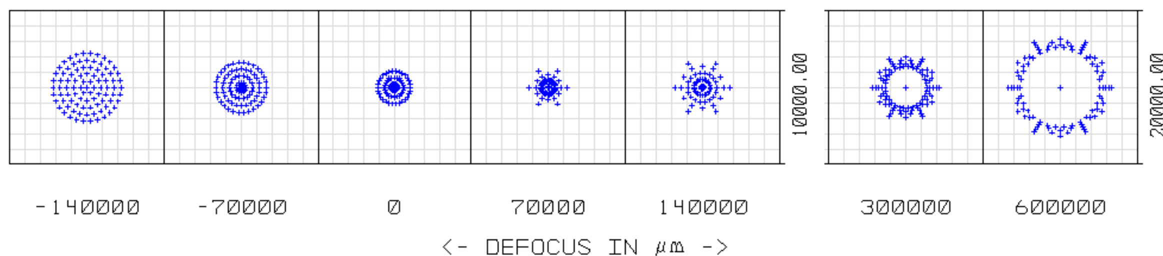

Figure 3.24. Through-focus analysis in ZEMAX for a Bessel beam of 1° axicon lens (wavelength is 1070 nm).

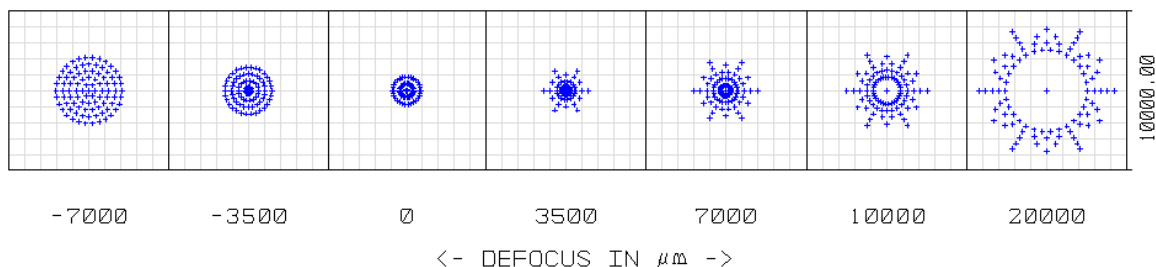

Figure 3.25. Through-focus analysis in ZEMAX for a Bessel beam of 20° axicon lens (wavelength is 1070 nm).

3.3.3.3. Beam Monitoring. Bessel Beam was profiled by a CCD camera with a microscopic lens system and by a Thorlabs beam profiler (BP209-IR) systematically by using a 1060 nm CW fiber laser source and a 633 nm HeNe laser system. Then the results were analyzed by MATLAB. Beam profiler was used in scanning-slit mode. Firstly, the center and the rings of the beam yielded by 1° was monitored as 3-D image, which can be seen in Figure 3.27. Thereafter, the transverse profile of the Bessel beam was prepared (Figure 3.28). As can be seen in the profile, the axicon lens with 1° base angle can produce a Bessel beam with 50 μm center radius for 1070 nm wavelength laser beam. Furthermore, the same laser beam was once more captured with a 20X magnification, and the result profile is shown in Figure 3.29.

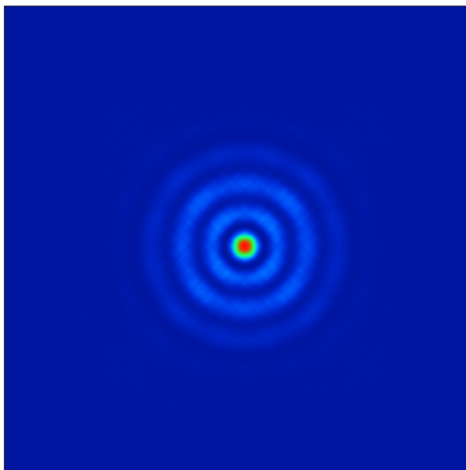

Figure 3.26. ZEMAX image of the radial distribution of a Bessel beam produced by 20° axicon lens (wavelength is 1070 nm).

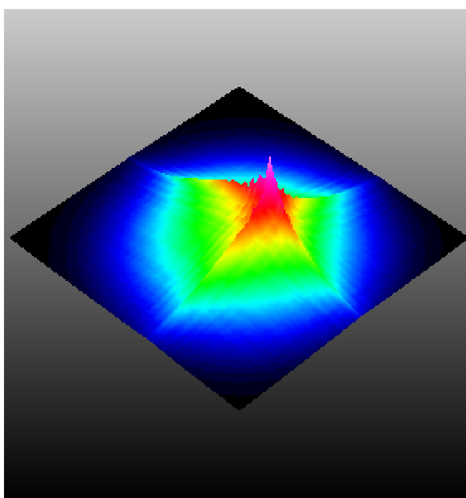

Figure 3.27. 3-D image of a Bessel beam produced by 1° axicon lens (wavelength is 1070 nm).

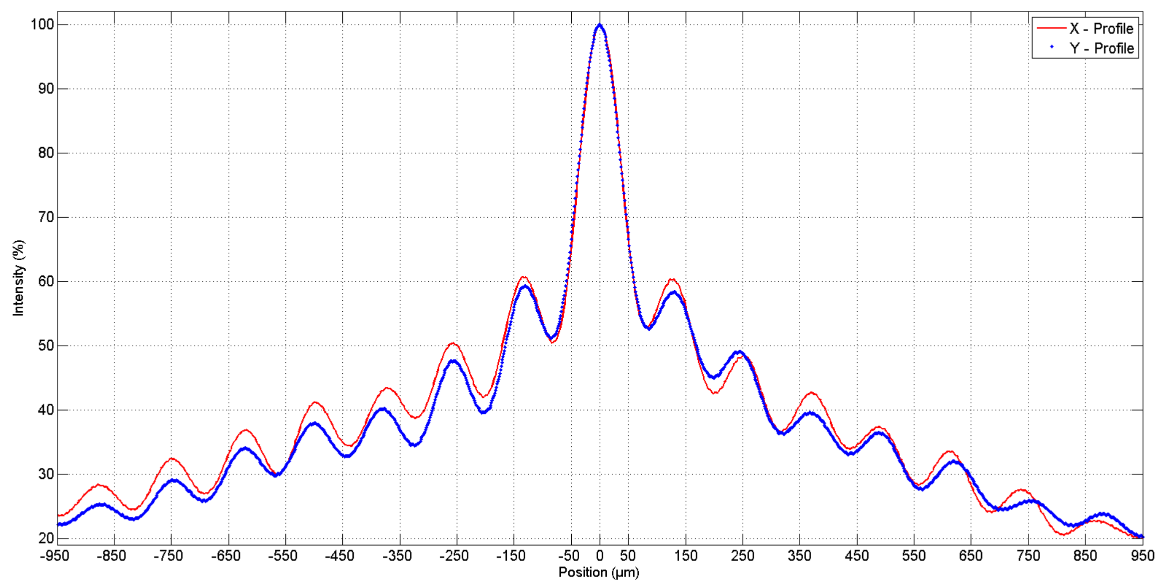

Figure 3.28. Transverse profile of the beam in Figure 3.27.

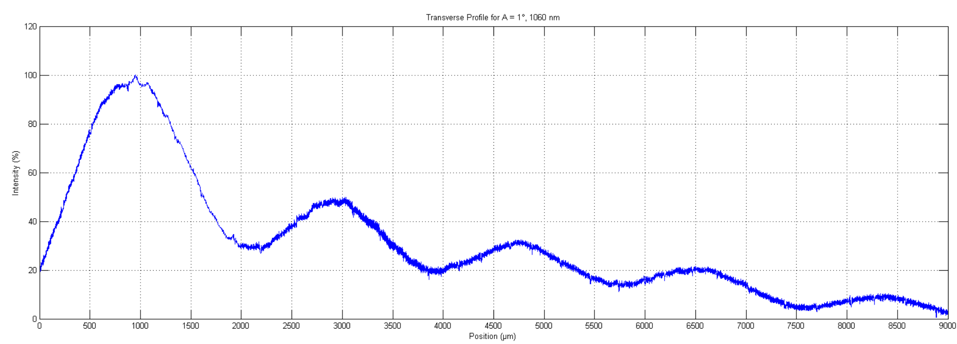

Figure 3.29. 20X magnification of the Bessel beam (1° axicon lens).

Moreover, the 20° axicon produced thinner Bessel beam rings with a smaller center spot than the 1° did, although the wavelength was different. By using HeNe laser source, the Bessel beam's transverse profile yielded by the 20°, acquired through the CCD image system, is demonstrated in Figure 3.30. And 1° produced bigger Bessel beam as Figure 3.31 displays (captured by CCD camera system).

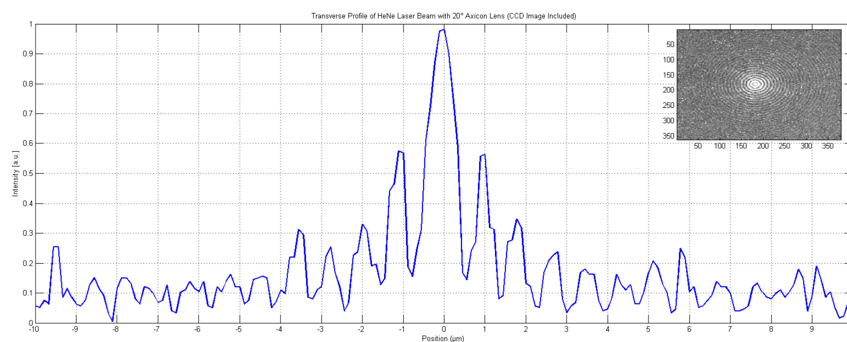

Figure 3.30. The transverse profile of a Bessel beam produced by 20° axicon at 633 nm wavelength (the graph contains the CCD image).

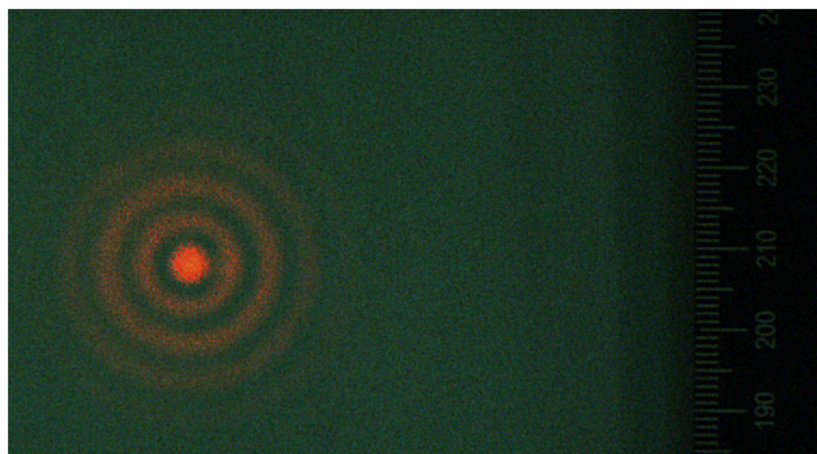

Figure 3.31. The CCD image of a Bessel beam produced by 1° axicon at 633 nm wavelength.

3.3.4. Experiments with Bessel Beams of Different Sizes

Laser-material interaction experiments continued with Bessel beams under the same conditions with previous experiments. Figure 3.32 shows a schematic of the experimental setup. The ns pulse laser beam propagates through a plano-concave (Thorlabs LC4252-B) and a plano-convex (Thorlabs LA4874-B) fused silica lens system, a high-power ND-YAG laser mirror (Edmund optics 33-076) and a mechanic shutter before it reaches the axicon lens. The cleaned and cleaved Si sample was put into the Bessel zone of the laser beam with a wavelength of 1070 nm. There is a two-dimensional translational stage under the Si sample. The experiments were carried out in a 100000 class cleanroom (ISO 8 class), and the temperature was 18°C, and the humidity was 50 % under stabilized conditions. Two different axicon lenses with 1° physical angle (Thorlabs AX251-B) and 20° physical angle (Thorlabs AX2520-B) were used in the experiments to reshape the Gaussian beam.

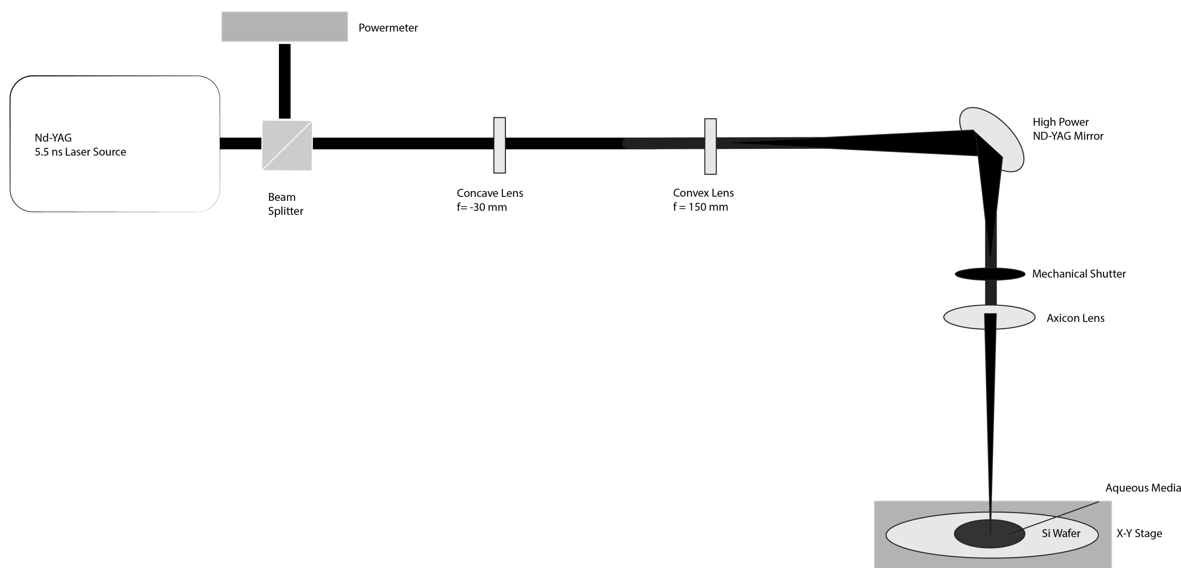

Figure 3.32. Experimental setup of Bessel beam-Si interaction studies.

Laser intensity and the number of pulses play a significant role in the laser induced micro-machining of the samples. The intensity, or in other words the fluence, can be modified either by the laser output energy or the beam spot diameter. In the laser

induced interaction process, the main problem is the loss of laser intensity due to the ambient absorbance, the beam divergence and the range of the depth of focus. Due to the fact that the Bessel beam propagates without any diffraction throughout the medium [40], it presents more advantages than a Gaussian beam in terms of the mentioned limitations. In case of a Gaussian beam profile, the sample location is so critical that the specimen must be placed in the beam waist delimited by the Rayleigh range. In some optical systems, the Rayleigh range may be so small, and the sample positioning becomes the main issue. Yet, a Bessel beam produced by an axicon lens does not diffract through the Bessel zone, therefore it maintains the fluence of the laser beam, and hence the sampling problem mostly disappears. Furthermore, the depth of focus of a Gaussian beam is much less than a Bessel beam with similar beam parameters of spot diameter, laser energy and wavelength.

In these experiments, two different Bessel beams were studied in order to observe the differences either between each other or between Bessel beam and Gaussian beam. Experiments with 1° axicon lens were carried out systematically in ambient and in liquid environments. However, 20° axicon lens studies were realized only in the air environment. Surface analyses were performed through OM, SEM and AFM measurement techniques.

3.3.4.1. Interaction of Bessel Beam Produced by 1° Axicon Lens. Thorlabs AX251-B axicon lens was used in these studies. The Bessel zone was approximately 400 mm, and the sample was placed at 145 mm distance after the axicon. The diameter of the central spot is 103.5 μm according to the results of theoretical and simulation calculations. The experiments were established in ambient conditions and then in water medium with a volume of 2400 mm^3. The effects of the laser's emission energy and pulse number were observed during the tests.

Interaction in Ambient Medium. Since the Bessel beam consists of the co-energetic rings, by reducing the average energy of the laser source, it is possible to minimize the occurrence of ablations caused by the ring. Initially, the relation between

the pulse energy and the ablation diameter is investigated through a single-pulse ablation. Figure 3.33 shows the damage areas after the illumination with a Bessel beam of the minimum (0.07 mJ) and maximum (82 mJ) laser energies. As can be seen in the images, while the high energetic rings are inducing ablations on the surface, in case of minimum energy, just the central spot leads to the damage in the sample. Figure 3.34 shows the relation between the pulse energy and the ablation diameter at the center. In comparison to the theoretical relation of the ablation diameter and the pulse energy, the experimental results also show a similar behavior, despite some deviations. Laser-induced damage threshold of p-type (111) Si sample is calculated as 75.45 mJ/cm^2 for a single pulse Bessel beam interaction. Furthermore, the depth of the ablation crater is measured, and the relationship between the pulse energy and the ablation depth is demonstrated in Figure 3.35.

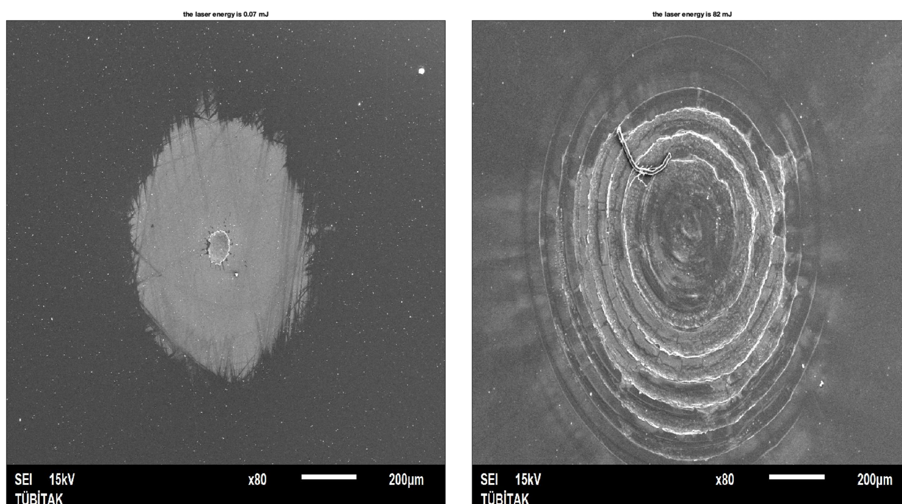

Figure 3.33. Laser damaged zones of the Si wafer after the interaction with the Bessel beams of minimum (left) and maximum (right) energy values.

Besides, the impact of multi-pulses on the Bessel beam interaction was examined by choosing a laser energy enough for a central damage but not enough for a ring's ablation. The laser output energy in this study was 9.8 mJ. In Figure 3.36 SEM images

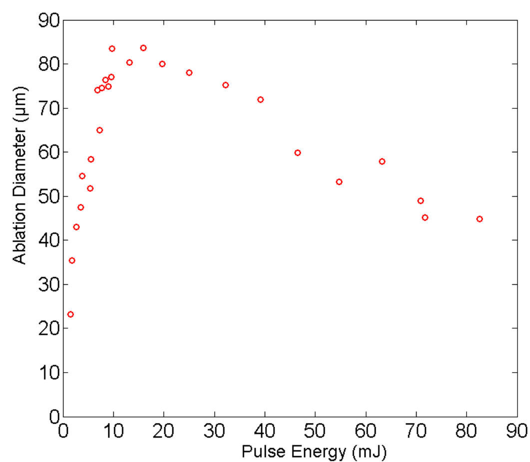

Figure 3.34. Ablation energy diameter vs pulse energy.

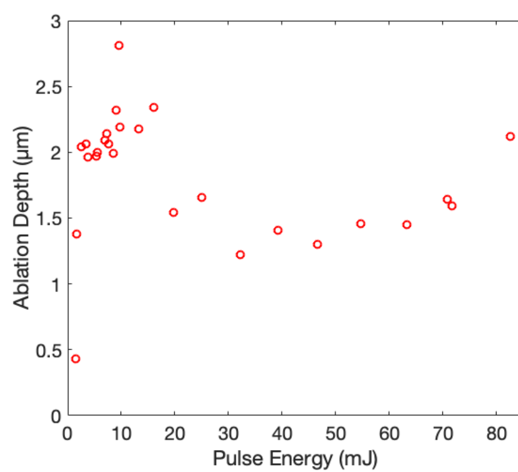

Figure 3.35. Ablation depth dependent on Bessel beam pulse energy.

of the ablation zones under exposure of 1, 40, 100 and 1000 pulses are demonstrated. The diameter of the ablation zone gets closer to the theoretically calculated beam diameter as seen in the graph (Figure 3.37). Finally, the depth of the ablation zone is also measured, as illustrated by Figure 3.38. The results indicate that, by changing the number of the pulse, it is possible to produce craters with a constant diameter but different depths.

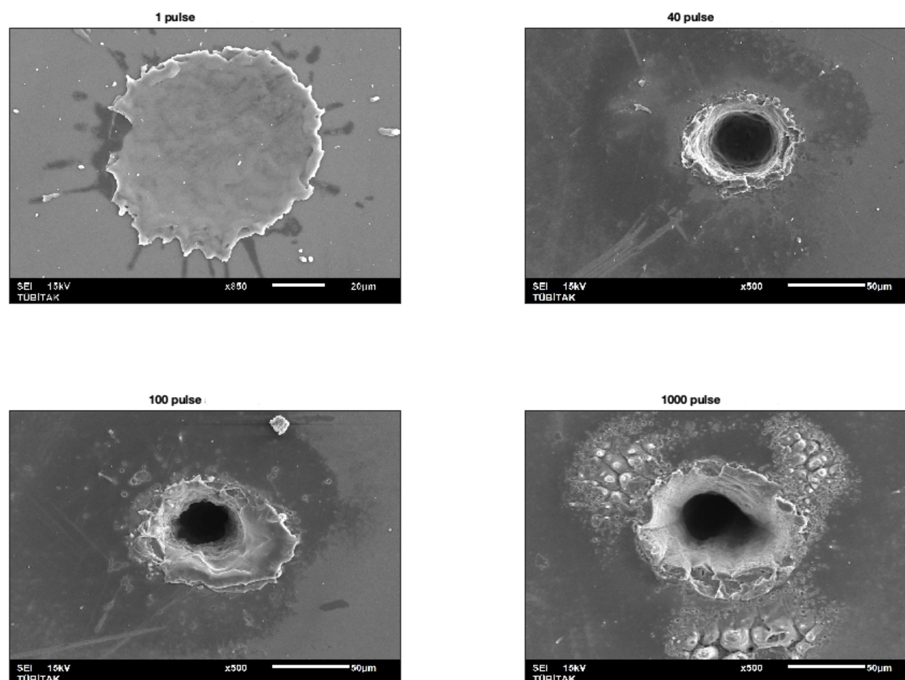

Figure 3.36. SEM images of the ablation zones produced by 1, 40, 100, 1000 pulses at an energy level of 9.8 mJ.

On the other hand, in the high energy Bessel beam ablation zones, the ripple and residual structure formations on the surface of (111) oriented p-type Si wafer were also observed (Figure 3.39).

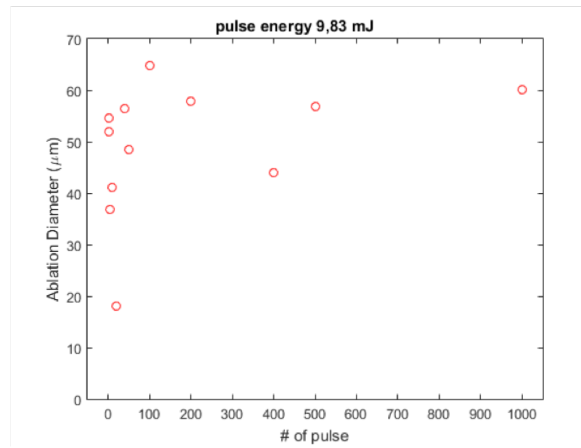

Figure 3.37. Ablation diameter for different number of pulses.

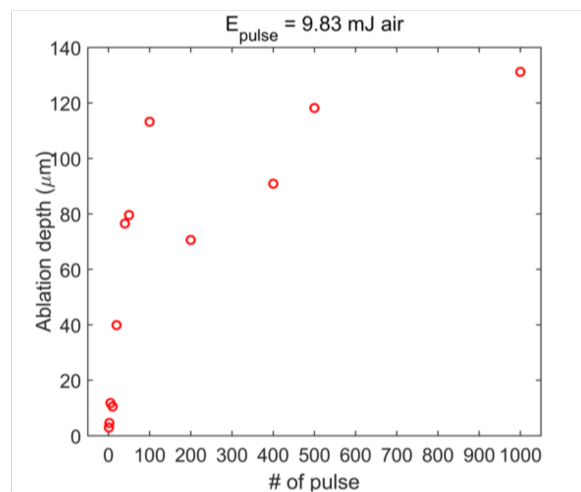

Figure 3.38. Ablation depth for different number of pulses.

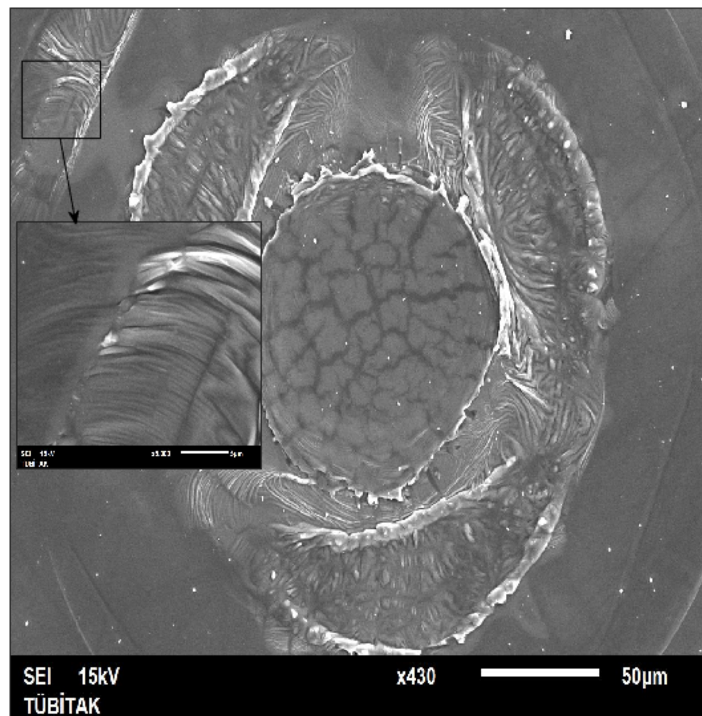

Figure 3.39. Ripple structures in the ablation zone on the surface of (111) p-type Si at a laser energy of 19.7 mJ .

Interaction in Water Medium. The studies in ambient conditions were repeated in the water medium systematically. Figure 3.40 shows a laser-induced damaged area after illumination of a Bessel beam with 40 mJ pulse energy, in which both the center and the rings affect the ablation production. In Figure 3.41, the ablation diameter was drawn based on the NIR ns single pulse Bessel beam energy. Also, Figure 3.42 illustrates the ablation crater depth versus the pulse energy. From the ablation diameter, the LIDT of Si is calculated as 98 mJ/cm^2, and the experimental results correlate with the theoretical values. Other than 2 distinct values, the depth of the craters are correlated as seen in the depth graph.

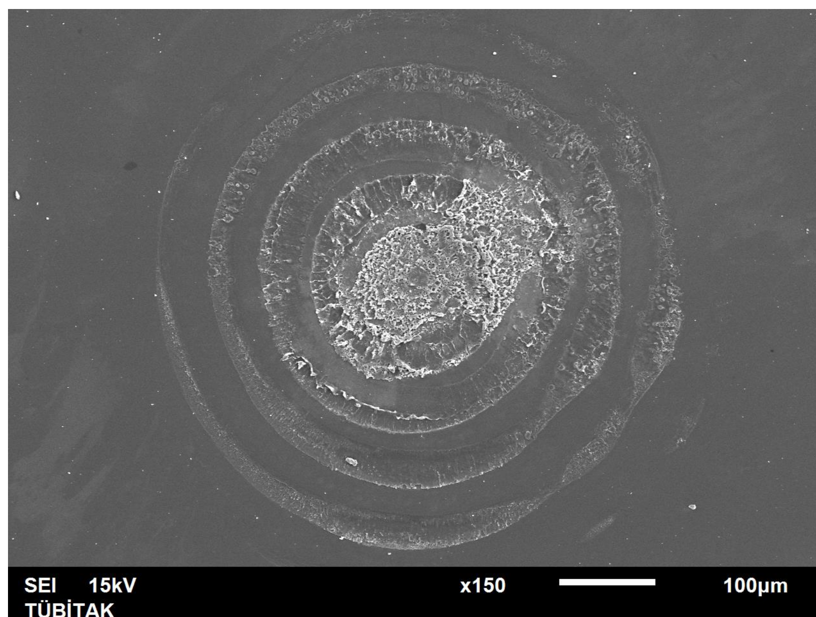

Figure 3.40. A sample damage area of the Bessel beam under water (pulse laser energy is 40 mJ).

The effect of the number of pulses on the ablation mechanism was observed in water medium. The pulse energy is constant at 9.8 mJ. At this energy level, only the central ablation occurs, the rings do not make any thermal or mechanical damage on the surface of Si sample. Figure 3.43 depicts the SEM images of 1, 10, 100 and 1000 pulses effects on the Si sample surface. In this case, the average ablation diameter is smaller than the beam spot diameter (Figure 3.44). Thereafter, depths of the ablation

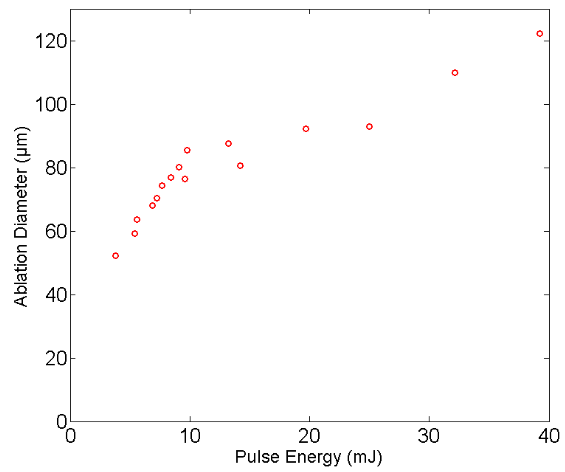

Figure 3.41. Diameter of ablation zones vs laser pulse energy under water.

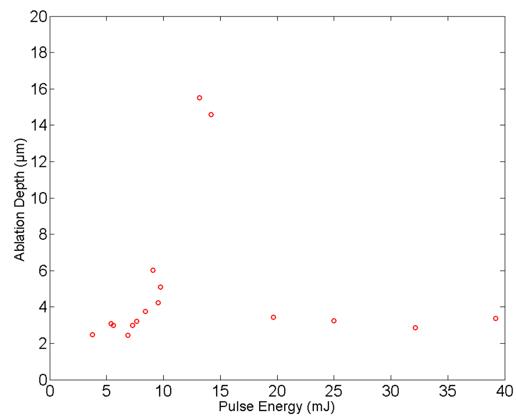

Figure 3.42. Depth of the ablation crater vs pulse energy under water.

zones are measured and graphed as seen in Figure 3.45

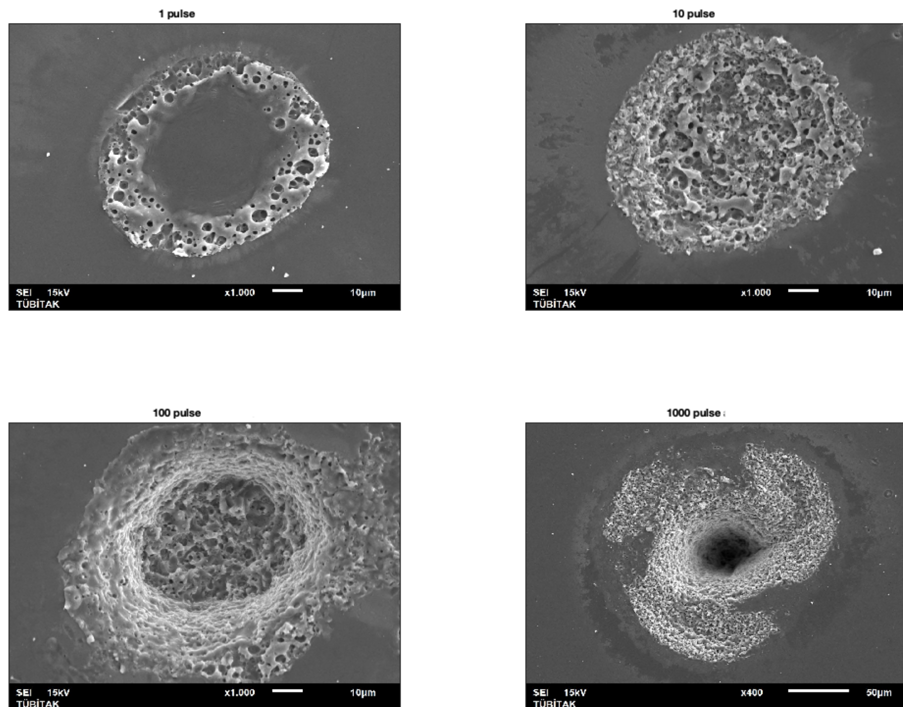

Figure 3.43. Damage areas produced by 1, 10, 100 and 1000 pulses. Bessel beam energy is 9.8 mJ.

<u>3.3.4.2. Interaction of Bessel Beam Produced by 20° Axicon Lens.</u> The Bessel beam studies were completed with the Thorlabs AX2520-B axicon lens. This axicon has 20° physical angle and produces a Bessel zone of approximately 20 mm long, and the center spot diameter is 4.8 μm. Firstly, the minimum energy range was researched to eliminate the contribution of Bessel rings to the ablation. By changing the energies of the single pulses, damaged areas on the sample surface were observed, and the diameter and depth of the crater were measured. Figures 3.46 and 3.47 are the AFM images of the laser induced damaged areas with minimum and maximum pulse energies respectively. Figure 3.48 exhibits the central ablation zone diameter as a function of single pulse laser energy. As expected, as the pulse energy increases, the size of the ablation zone

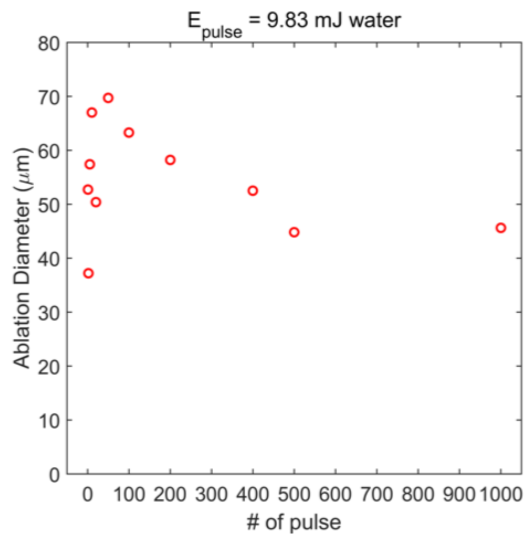

Figure 3.44. Diameter of the ablation zone vs. number of pulses in water ambient.

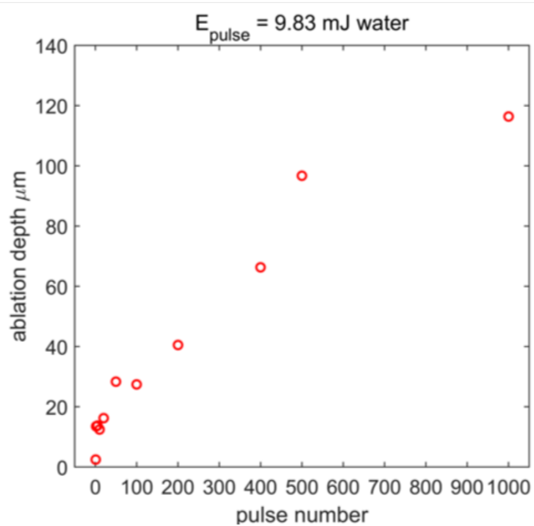

Figure 3.45. Depth of the ablation zone vs. the number of pulses in water ambient.

also gets bigger. On the other hand, the depths of central ablation areas are given in Figure 3.49.

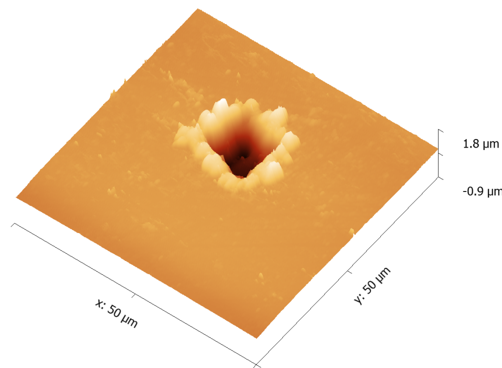

Figure 3.46. AFM image of the minimum ablation area on the Si sample surface after illumination with Bessel beam (20° axicon).

Moreover, multi-pulse study is also handled in 20° axicon lenses at several energy values. The SEM image of Figure 3.50 shows the effects of 1, 5, 200 and 1000 pulses on the surface of the Si sample, where the laser beam energy is 14 mJ. Then, diameters of ablation zones and depths of craters were also measured. According to ablation diameter measurements, as the number of pulses increases, the diameter of the laser-induced area approaches up to the twofold of beam diameters. This conclusion is valid for 5 different pulse energy values including 28.5 mJ, 25 mJ, 22.4 mJ, 19.7 mJ and 14.2 mJ (Figure 3.51). On the other hand, as the number of pulses increases, the depth of ablation craters also rises (Figure 3.52).

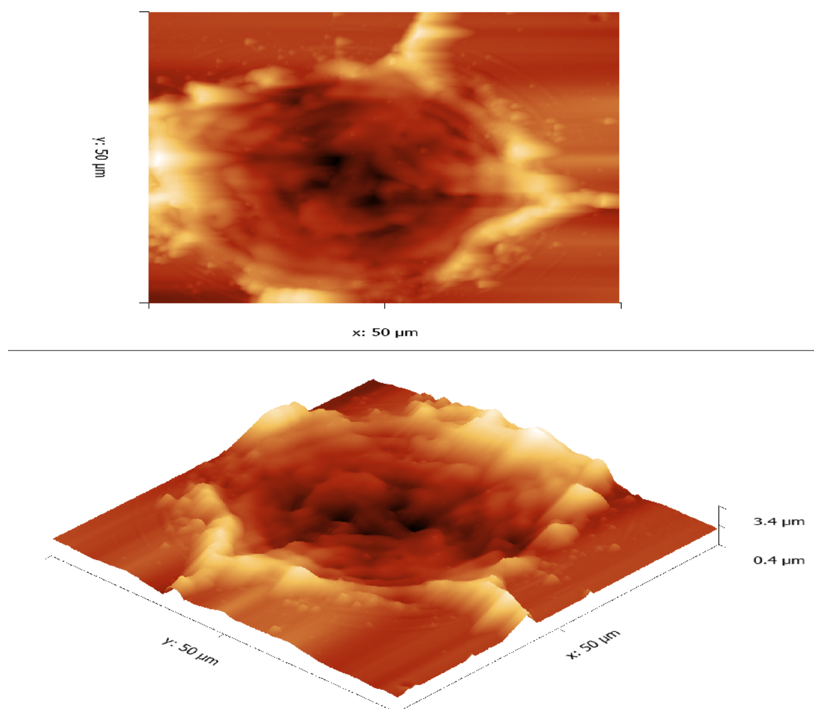

Figure 3.47. 2-D and 3-D AFM images of the maximum ablation area on the Si sample.

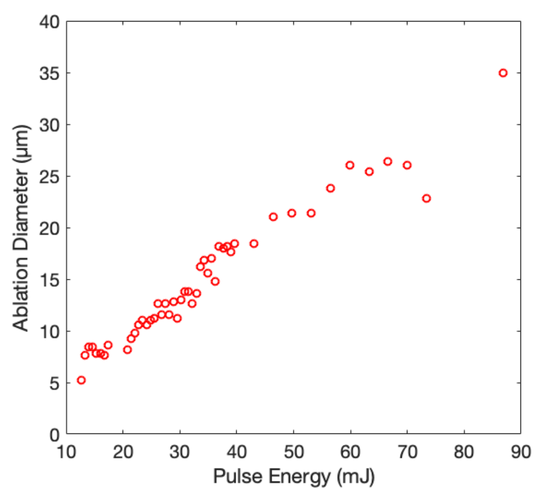

Figure 3.48. Ablation diameters vs. Bessel beam pulse energies.

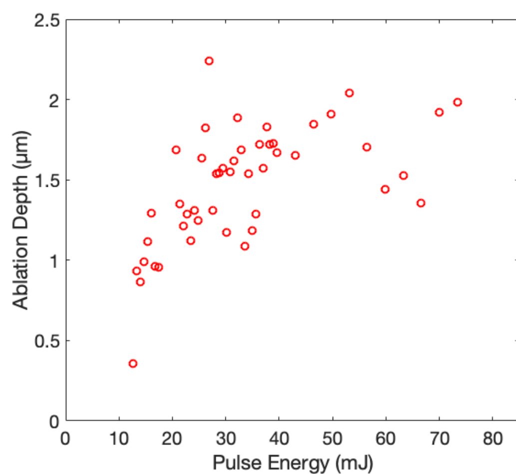

Figure 3.49. Depths of ablation zones vs. Bessel beam pulse energies.

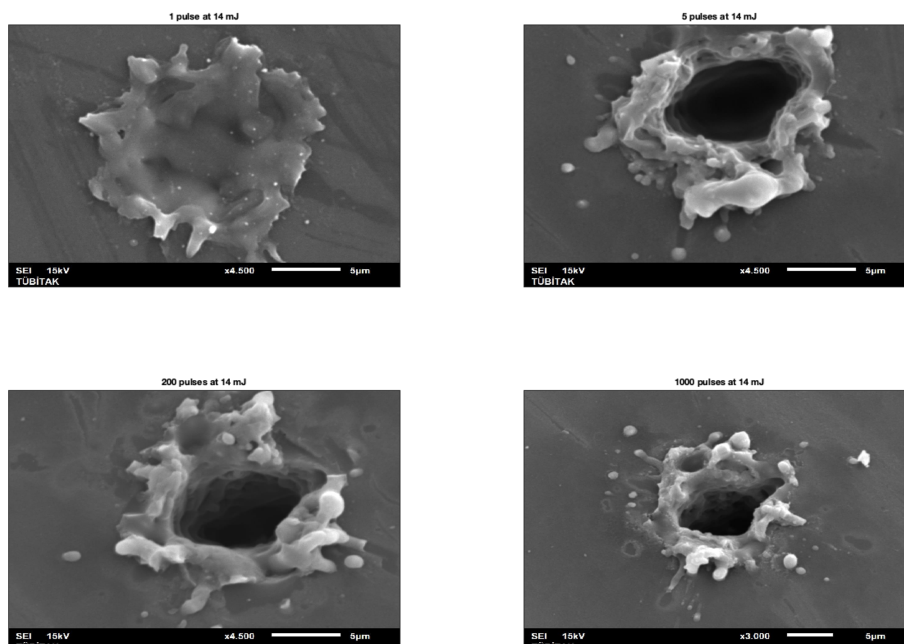

Figure 3.50. SEM images of ablation zones for different number of pulses at 14 mJ.

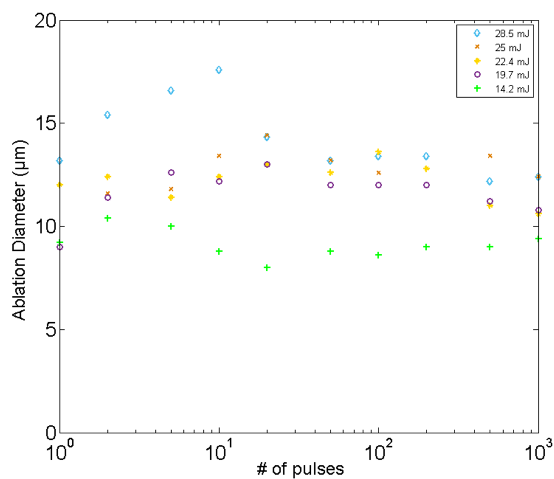

Figure 3.51. Diameters of ablation zones vs. the number of Bessel beam pulses.

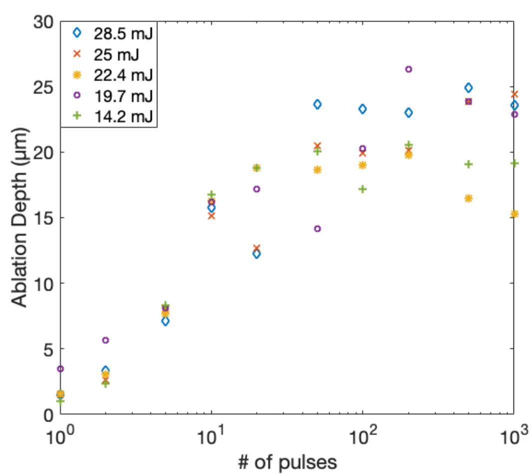

Figure 3.52. Depths of ablations vs. the number of Bessel beam pulses.

3.3.4.3. Comparison of the Results. Under illumination of 1070 nm pulse laser source, the surface morphology of p-type Si wafer depending on the Bessel beam profile and sample environment was observed. Two kinds of axicon lenses were used to reform the incoming Gaussian laser beam. Firstly, the surface micro-structuring studies were handled by 1° axicon lens yielding a Bessel beam with 104 μm center diameter and 400 mm Bessel zone. Ablation diameter and depth were calculated in ambient and water conditions, respectively. Besides, the effects of multi-pulses on the Si specimen structure were also investigated in different environments. According to the results acquired both in air and water, NIR ns pulse laser beam with Bessel distribution produces an ablation crater with a diameter equal to or less than the central spot of the Bessel beam. One main reason for this may be the non-diffracted distribution of the Bessel beam. In addition, rings exhibit thermal spread around the surface. Figure 3.53 shows the comparison of the damage areas under air and water environments. As can be seen in the Figure, as the power of laser beam decreases, the damage areas get smaller and the contribution of the rings to the ablation disappears. On the other hand, in liquid medium, it seems possible to increase the absorbance of the Si sample, because the structured surface becomes like a black silicon. In addition, any ripple or residual formations were not observed in laser induced ablation zones in water medium.

Ambient | Water

240

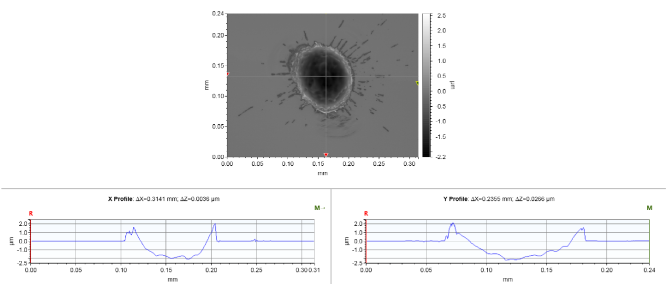

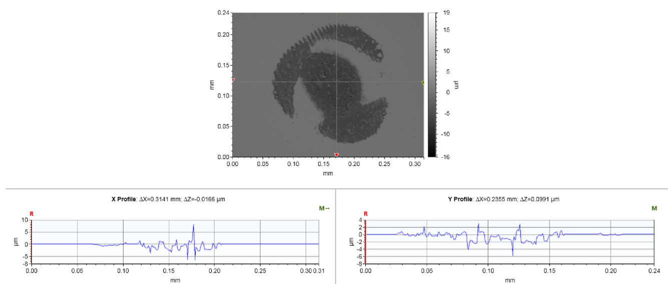

244

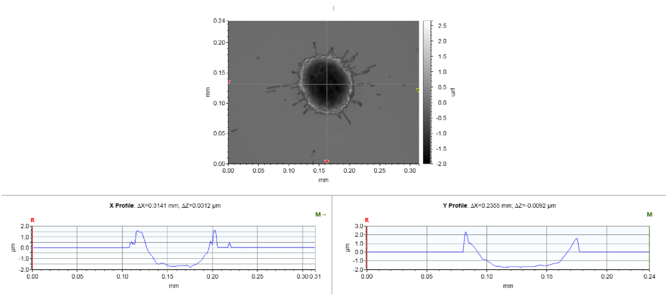

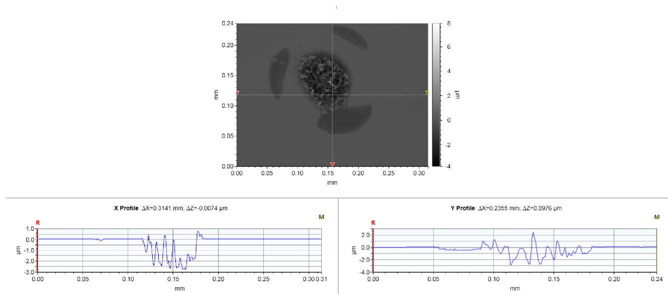

250

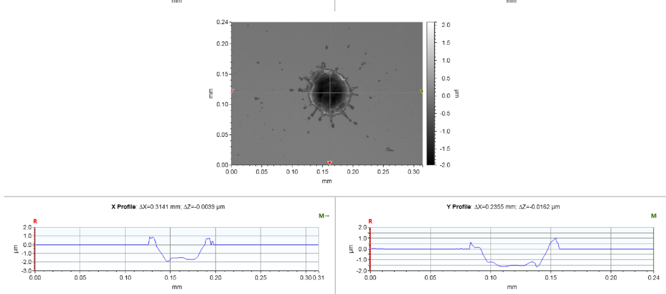

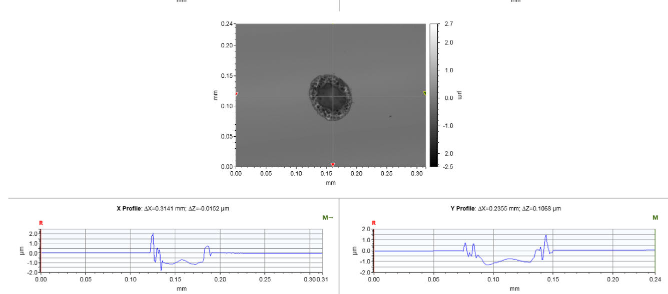

Figure 3.53. OM images of Bessel beam induced ablation zones in ambient and water media .

Thereafter, studies proceeded with an axicon lens 20°, and their results were compared with those of the previous studies. The beam diameter is 4.8 μm and the length of the Bessel zone is 20 mm. Ablation zones in 20° are significantly smaller than the damaged areas in 1°. While the high energetic rings of the Bessel beam produce some ablations on the Si sample surface, at lower energy levels, only the central spot causes the sample to ablate. Experimentally, in comparison to 1° axicon lens, the energy of the minimum damaged point is higher in 20° axicon lens. In fact, while the beam diameter shrinks, the damage threshold increases. This makes sense, because the fluence of the laser beam is negatively proportional to the beam diameter square. Moreover, in case of so small beam spots, air ionization and plasmic interaction may occur in front of the sample surface, which may lead to extra air absorption of laser beam. As a result, the beam fluence falling upon the surface of the sample decreases due to the plasmic absorptions. On the other hand, the reflection of the sample increases as the beam spot gets smaller.

Furthermore, the number of pulses plays an important role on the surface manufacturing by laser inducing. In these experiments, p-type (111) Si sample is illuminated by different number of pulses with identical levels of pulse energy. According to the measurements of ablation diameter and depth, firstly as number of pulse increases, the ablation diameter also increases. However, after a certain number of pulse, while the number of pulses increases, the diameter of the ablation zone remains almost unchanged and the depth of crater increases. As a conclusion, it can be said that the depth of crater can be systematically controlled by increasing the number of pulses at a constant pulse energy.

Finally, in the ablation zones produced by Bessel beams, ablation diameters are closer to the central diameter of the Bessel beam. In case of Gaussian beams, due to the thermal effects, ablation diameters became a little bit higher than the spot size even though they are in the same order. In both Gaussian beam and Bessel beam experiments, the residual effect formation (debris, ripples, etc.) between ablation zone and the HAZ were observed in air medium. Yet, in both cases, these effects vanished in water medium.

Additionally, EDX analysis on the ablation zones were also performed for different beam profile ablation studies under ambient conditions. In case of Gaussian beam interaction with Si wafer, while 96.1 % of the surface is Si, only 3.9 % of it is Oxygen. On the other hand, in ablation zone yielded by a Bessel beam of 20° axicon, the Oxygen percentage decreases (97.6 % Si, 2.4 % O).

4. CONCLUSION

In this study, the interaction mechanism of 1070 nm laser source with monocrystalline Si wafer was examined. In particular, laser emission type, pulse energy, number of pulses, beam shape and ambient conditions were investigated throughout the experiments. Initially, laser beams were monitored by both CCD camera and beam profiler. Then, Si wafer optical properties in terms of reflectance and transmittance were measured to use them in the calculations of the optical constant. After experimental operations, surface analyses were performed through OM, SEM and AFM.

CW laser induced damage areas on the surface of p-type and n-type Si wafers included partially molten and totally molten zones. Besides, there was a crack zone which could be caused by slips of the wafer planes and it differed depending on Si wafer type.

Ns laser induced areas of p-type Si wafer still contained HAZ around ablation craters, including self-assembly ripple formations and residual effects. In liquid medium, however, the occurrence of HAZ areas got smaller in water or even completely vanished in glycerin. Furthermore, the beam shape of the laser beam on the micro-machining process produced differences in terms of HAZ formations and ablation diameters. Regardless of beam shape and environment, the ablation diameter became larger as the laser beam emission energy increased. Finally, as the number of pulses increased, the depth of ablation crater also augmented, but there was no significant change in the diameter of the ablation crater.

To continue with, the experiments show that it is possible to make controlled ablation zones in a (111) Si wafer with a ns laser source. Therefore, the next step will be to continue with the production of vessels on the Si sample surface in line with the requirements of the SC industry. In addition, these vessels may be used in production of systematic coating of Si wafers with different types of polymer. Moreover, production of nano-particles by laser illumination will be studied, because laser induced production

provides green synthesis of nano-particles, thereby presenting the opportunity of toxic-free operation.

REFERENCES

1. Nestor, M., A. Andriessen, B. Berman, B. E. Katz, D. Gilbert, D. J. Goldberg, M. H. Gold, R. S. Kirsner and P. Z. Lorenc, "Photobiomodulation with non-thermal lasers: Mechanisms of action and therapeutic uses in dermatology and aesthetic medicine", *Journal of Cosmetic and Laser Therapy*, Vol. 19, No. 4, pp. 190–198, 2017, `https://doi.org/10.1080/14764172.2017.1293828`, pMID: 28328287.

2. Nugent, T. J. and J. T. Kare, "Laser power beaming for defense and security applications", 2011, `https://doi.org/10.1117/12.886169`.

3. Qin, Y., A. Brockett, Y. Ma, A. Razali, J. Zhao, C. Harrison, W. Pan, X. Dai and D. Loziak, "Micro-manufacturing: research, technology outcomes and development issues", *The International Journal of Advanced Manufacturing Technology*, Vol. 47, No. 9, pp. 821–837, Apr 2010, `https://doi.org/10.1007/s00170-009-2411-2`.

4. Tull, B. R., J. E. Carey, E. Mazur, J. P. McDonald and S. M. Yalisove, "Silicon surface morphologies after femtosecond laser irradiation", *MRS Bulletin*, Vol. 31, No. 8, pp. 626–633, 2006.

5. Trtica, M. S., B. M. Gakovic, D. Maravic, D. Batani, T. Desai and R. Redaelli, "Surface modifications of crystalline silicon created by high intensity 1064 nm picosecond Nd:YAG laser pulses", *Applied Surface Science*, Vol. 253, No. 24, pp. 9315–9318, 2007.

6. Zhou, Y., B. Wu, S. Tao, A. Forsman and Y. Gao, "Physical mechanism of silicon ablation with long nanosecond laser pulses at 1064nm through time-resolved observation", *Applied Surface Science*, Vol. 257, No. 7, pp. 2886–2890, 2011.

7. Wang, X., D. Zhu, Z. Shen, J. Lu and X. Ni, "Surface damage morphology investigations of silicon under millisecond laser irradiation", *Applied Surface Science*, Vol. 257, pp. 1593–1588, September 2010.

8. Kim, K.-R., T.-H. Kim, H.-A. Park, S.-Y. Kim, S.-H. Cho, J. Yi and B.-D. Choi, "UV laser direct texturing for high efficiency multicrystalline silicon solar cell.", *Applied Surface Science*, Vol. 264, pp. 404–409, 2013.

9. Li, K., M. Sparkes and W. O'Neill, "Comparison Between Single Shot Micromachining of Silicon with Nanosecond Pulse Shaped IR Fiber Laser and DPSS UV Laser", *IEEE Journal of Selected Topics in Quantum Electronics*, Vol. 20, No. 5, 2014.

10. Bonse, J., K. Brzezinka and A.J.Meixner, "Modifying single-crystalline silicon by femtosecond laser pulses: an analysis by micro Raman spectroscopy, scanning laser microscopy and atomic force microscopy", *Applied Surface Science*, Vol. 221, pp. 215–230, 2004.

11. Armbruster, O., A. Naghilou, M. Kitzler and W. Kautek, "Spot size and pulse number dependence of femtosecond laser ablation thresholds of silicon and stainless steel", *Applied Surface Science*, Vol. 396, pp. 1736–1740, 2017.

12. Wu, S., *Femtosecond laser micro-structuring of silicon wafer in water confinement*, Master thesis, Missouri University of Science and Technology, 2008.

13. Watanable, S., Y. Yoshida, S. Kayashima, S. Yatsu, M. Kawai and T. Kato, "In situ observation of self-organizing nanodot formation under nano-second pulse laser irradiation on Si surface", *Journal of Applied Physics*, Vol. 108, No. 10, 2010.

14. Karnakis, D. M., "High power single-shot laser ablation of silicon with nanosecond 355 nm", *Applied Surface Science*, Vol. 252, No. 2, pp. 7823–7825, 2006.

15. Klotzbach, U., A. Lasagni, M. Panzner and V. Franke, *Laser Micromachining*, Vol. 10, pp. 29–46, Springer Berlin Heidelberg, 01 1970.

16. Demirci, E., E. T. Akşit Kaya and R. Şahin, "Nanosecond laser ablation of Si(111) under an aqueous medium", *Optik*, Vol. 181, pp. 1049–1056, December 2018.

17. Middlebury College, "*The Helium-Neon Laser*", 1992-93, https://bit.ly/2Wk8S8Q, accessed at May 2019.

18. Kleine, K. F. and K. G. Watkins, "Fiber laser for micro-cutting of metals", 2003, https://doi.org/10.1117/12.484171.

19. Maclean, J. O., J. Hodson, C. Tangkijcharoenchai, S. Al-Ojaili, S. Rodsavas, S. Coomber and K. Voisey, "Laser drilling of microholes in single crystal silicon using continuous wave (CW) 1070 nm fiber lasers with millisecond pulse widths", *Lasers in Engineering*, Vol. 39, No. 1-2, pp. 53–65, March 2018, http://eprints.nottingham.ac.uk/49169/.

20. Hendow, S. T. and S. A. Shakir, "Structuring materials with nanosecond laser pulses", *Opt. Express*, Vol. 18, No. 10, pp. 10188–10199, May 2010, http://www.opticsexpress.org/abstract.cfm?URI=oe-18-10-10188.

21. O'Mara, W., R. B. Herring and L. P. Hunt, *Handbook of Semiconductor Silicon Technology*, Crest Publishing House, South Africa, 2007.

22. Zhu, S., Y. F. Lu, M. H. Hong and X. Y. Chen, "Laser ablation of solid substrates in water and ambient air", *Journal of Applied Physics*, Vol. 89, No. 4, pp. 2400–2403, 2001, https://doi.org/10.1063/1.1342200.

23. Schinke, C., P. Christian Peest, J. Schmidt, R. Brendel, K. Bothe, M. R. Vogt, I. Kröger, S. Winter, A. Schirmacher, S. Lim, H. T. Nguyen and D. MacDonald, "Uncertainty analysis for the coefficient of band-to-band absorption of crystalline silicon", *AIP Advances*, Vol. 5, No. 6, p. 067168, 2015, https://doi.org/10.1063/1.4923379.

24. Brown, M. S. and C. B. Arnold, *Fundamentals of Laser-Material Interaction and Application to Multiscale Surface Modification*, pp. 91–120, Springer Berlin Heidelberg, Berlin, Heidelberg, 2010, https://doi.org/10.1007/978-3-642-10523-4_4.

25. Lucas, L. and J. Zhang, "*Femtosecond laser micromachining: A back-to-basics primer*", 01 2012, `https://bit.ly/2w9ofSN`, accessed at May 2019.

26. Ngoi, B., K. Venkatakrishnan, E. Lim, B. Tan and L. Koh, "Effect of energy above laser-induced damage thresholds in the micromachining of silicon by femtosecond pulse laser", *Optics and Lasers in Engineering*, Vol. 35, No. 6, pp. 361–369, February 2001.

27. Tran, D., H. Zheng, Y. Lam, V. Murukeshan, J. Chai and D.E.Hardt, "Femtosecond laser-induced damage morphologies of crystalline silicon by sub-threshold pulses", *Optics and Lasers in Engineering*, Vol. 43, No. 9, pp. 977–986, September 2005.

28. Talbi, A., A. Petit, A. Melhem, A. Stolz, C. Boulmer-Leborgne, G. Gautier, T. Defforge and N. Semmar, "Nanoparticles based laser-induced surface structures formation on mesoporous silicon by picosecond laser beam interaction", *Applied Surface Science*, Vol. 374, pp. 31–35, June 2016.

29. Lin, Y.-T., *Femtosecond-laser hyperdoping and texturing of silicon for photovoltaic applications*, Doctoral dissertation, Harvard University, 2014, `http://nrs.harvard.edu/urn-3:HUL.InstRepos:12274579`.

30. Xia, Y., B. Liu, J. Liu, Z. Shen and C. Li, "A novel method to produce black silicon for solar cells", *Solar Energy*, Vol. 85, No. 7, pp. 1574–1578, July 2011.

31. Jansen, H. V., M. J. de Boer, R. Legtenberg, R. Legtenberg and M. C. Elwenspoek, "The black silicon method: A universal method for determining the parameter setting of a fluorine-based reactive ion etcher in deep silicon trench etching with profile control", *Journal of micromechanics and microengineering*, Vol. 5, pp. 115–120, 6 1995.

32. Sarnet, T, T. J. Derrien, R. Torres, P. Delaporte, F. Torregrosa, M.J. Sher, Y. T. Lin, B. Franta, G. Deng and E. Mazur, "Black Silicon for Photovoltaic Cells: Towards a High-efficiency Silicon Solar Cell", *EU PVSEC Proceedings,* 10 2013.

33. Chi, S. and K.-Y. Jhang, "Thermal damages on the surface of a silicon wafer induced by a near-infrared laser", *Optical Engineering*, Vol. 53, No. 1, pp. 017103–1–7, January 2014.

34. Jia, Z.-C., Z.-W. Li, J. Zhou and X.-W. Ni, "Slip on the surface wafers under laser irradiation: Scale effect", *Chin. Phys. B*, Vol. 26, No. 11, pp. 116102–1–116102–6, September 2017.

35. Wang, X., Y. Qin, Z. W. Li, H. C. Zhang, Z. H. Shen and X. W. Ni, "The Interaction and the Surface Crack of Single-Crystal Silicon Induced by a Millisecond Laser", *Surface Phenomena*, Vol. 22, No. 10, pp. 1627–1634, September 2012.

36. Mannion, P., J. Magee, E. Coyne, G. O'Connor and T. Glynn, "The effect of damage accumulation behaviour on ablation thresholds and damage morphology in ultrafast laser micro-machining of common metals in air", *Applied Surface Science*, Vol. 233, No. 1–4, pp. 275–287, 2004.

37. Venkatakrishnan, K., P. Stanley, N. Sivakumar, B. tan and L. Lim, "Effect of scanning resolution of thin films", *Applied Physics A- Materials Science Processing*, Vol. 77, No. 5, pp. 655–658, 2003.

38. Karimzadeh, R., J. Zamir-Anvari and N. Mansour, "Nanosecond pulsed laser ablation of silicon in liquids", *Applied Physics A*, Vol. 94, pp. 949–955, September 2008.

39. Phipps, C. R. (Editor), *Accumulation effects in laser ablation of metals with high-repetition-rate lasers*, Vol. 7005, SPEI, 2008.

40. Şahin, R., *Femtosaniye Lazer Ablasyonu ile İnce Filmler Üzerinde Nano-Yapılandırma ve Karakterizasyon*, Ph.D. Thesis, İTÜ, October 2014.

41. Demirci, E., E. T. Akşit Kaya and R. Şahin, "Bessel laser beam interaction with Si(111) wafer", December 2019, will be published.

42. Self, S. A., "Focusing of spherical Gaussian beams", *Appl. Opt.*, Vol. 22, No. 5, pp. 658–661, Mar 1983, http://ao.osa.org/abstract.cfm?URI=ao-22-5-658.

43. Labsphere, *Reflectance and Transmittance Measurements Integrating Spheres*, Lab-sphere, 3 edn.

44. Ravindra, N. M., B. Sopori, O. H. Gokce, S. X. Cheng, A. Shenoy, L. Jin, S. Abedrabbo, W. Chen and Y. Zhang, "Emissivity Measurements and Modeling of Silicon-Related Materials: An Overview", *International Journal of Thermophysics*, Vol. 22, No. 5, pp. 1593–1611, September 2001.